

Macroelement Model for the Progressive-Collapse Analysis of Infilled Frames

*Original*

Macroelement Model for the Progressive-Collapse Analysis of Infilled Frames / Di Trapani, F.; Tomaselli, G.; Cavaleri, L.; Bertagnoli, G.. - In: JOURNAL OF STRUCTURAL ENGINEERING. - ISSN 0733-9445. - STAMPA. - 147:6(2021), pp. 1-19. [10.1061/(ASCE)ST.1943-541X.0003014]

*Availability:*

This version is available at: 11583/2904494 since: 2025-02-12T13:17:54Z

*Publisher:*

American Society of Civil Engineers (ASCE)

*Published*

DOI:10.1061/(ASCE)ST.1943-541X.0003014

*Terms of use:*

This article is made available under terms and conditions as specified in the corresponding bibliographic description in the repository

*Publisher copyright*

ASCE postprint/Author's Accepted Manuscript

This material may be downloaded for personal use only. Any other use requires prior permission of the American Society of Civil Engineers. This material may be found at [http://dx.doi.org/10.1061/\(ASCE\)ST.1943-541X.0003014](http://dx.doi.org/10.1061/(ASCE)ST.1943-541X.0003014).

(Article begins on next page)



## 35 **Introduction**

36 Progressive collapse analysis and robust design of structures and infrastructures are emerging as hot  
37 topics in the last years for both researchers and practitioners. This is not only highlighted by the recent  
38 increase of numerical and experimental studies, but also the general directions of the latest updates  
39 of most of the technical codes indicate robustness as a trait of new construction (**Marchand and**  
40 **Stevens, 2016, Adam et al., 2018**), following the basic principle of robustness-based design  
41 according to which, the effect of an accidental damage suffered by a structure, would not be  
42 disproportionate with respect to the cause that generated it. For what concerns reinforced concrete  
43 frame building structures, the most critical condition inducing progressive collapse is generally  
44 related to the loss of a base column due, for instance, to impacts or explosions. In these condition  
45 vertical loads, and the arising inertial forces, are rapidly redistributed to the adjacent structural  
46 elements, the damage mechanism involves the beams converging to the column, which develop a  
47 resisting mechanism evolving in three sequential steps: a) a flexural resistant mechanism; b) a post-  
48 cracking arching mechanism; c) a catenary mechanism, triggering a large displacements regime  
49 (**Izzuddin et al., 2008, Weng et al., 2017**). The damage evolution is accentuated by the effect of  
50 gravity inertial forces arising and can be stopped within one of these three phases only if adequate  
51 resistance supply is available to achieve a new equilibrium configuration. Otherwise, collapse of the  
52 spans above the collapsed column occurs, also undermining the overall stability. Several authors have  
53 carried out studies concerning theoretical and practical assessment of this kind of progressive collapse  
54 response for frame structures. Among these **Izzuddin et al. (2008)** and **Vlassis et al., 2008** provided  
55 an effective method for the simplified evaluation of dynamic load-displacement demand, through a  
56 pseudo-static approach based on the energy balance between internal and external work for the  
57 substructural levels involved in the collapse mechanism. More recently experimental tests were  
58 carried out on scaled size structural elements (**Ren et al., 2016**) and structures (**Xiao et al., 2015**).  
59 Other experimental studies, accompanied by numerical interpretations (**Yu and Tan (2013), Pham**  
60 **et al. (2015), Pham et al. (2017)** and **Weng et al. (2017)**) have investigated the fundamental

61 geometrical and mechanical aspects influencing the progressive collapse response of RC structures,  
62 providing also effective modelling strategies. A comprehensive state of the art illustrating the latest  
63 advances on gravity-induced collapse modeling for reinforced concrete structures has been also  
64 provided by **Kunnath et al. (2018)**. The major findings of the aforementioned studies report that the  
65 ductility of the beam end cross-sections plays a prominent role on the activation capacity of the  
66 catenary mechanism, but also that this is conditioned by many other factors such as the horizontal  
67 constraint degree as well as the real capacity of elongation of steel.

68 On the other hand, more recent studies, have demonstrated from the experimental and numerical point  
69 of view that the gravity-induced progressive collapse mechanism of frame structures is significantly  
70 altered by the presence of masonry infills (**Farazman et al., 2013, Xavier et al., 2015, Shan et al.,**  
71 **2016, Qian et al., 2017, Li et al., 2019, Di Trapani et al 2020a**). Therefore, the interaction between  
72 frames and infills due to lateral loads, which has been widely investigated in the past by experimental  
73 quasi-static tests (e.g. **Mehrabi et al. 1996, Colangelo 2005, , Kakaletsis, Karayannis 2009, Calvi**  
74 **and Bolognini 2001, Morandi et al. 2018**) and numerical studies addressing micro-modelling (e.g.  
75 **Mehrabi et al. 1997, Stavridis and Shing 2010, Calì & Pantò 2014**) and equivalent single or  
76 multi-strut macro modelling (e.g. **Panagiotakos and Fardis 1996, El-Dakhkhni et al. 2003,**  
77 **Crisafulli and Carr 2007, Furtado et al., 2015, Di Trapani et al. 2020b**) also occurs in the case of  
78 gravity-induced progressive collapse. This has noticeable impact to the overall resistance increase,  
79 accompanied by a less prominent post-peak response and reduced propension in developing the  
80 catenary mechanism under the large displacement regime in comparison with bare frames. As a  
81 secondary effect, the increase in strength is also associated with a stiffness increment, causing an  
82 increase of the dynamic amplification factor (**Di Trapani et al., 2020a**). Therefore, the infilled frame  
83 has more resistance but, at the same time, the dynamic load demand increases too.

84 These premises make evident that progressive collapse of infilled frames cannot be assessed properly  
85 without an adequate modeling of frame-infill interaction. In particular, a simplified modelling  
86 strategy comes out as fundamental need to effectively assess progressive collapse response of infilled

87 frames, although available experimental tests are still limited. Also for this reason, the proposed  
88 simplified macro-modeling approaches are theoretically based (e.g. **Farazman et al., 2013**) or not  
89 entirely generalizable, being validated on single experiments (e.g. **Li et al., 2019**). In a recent paper,  
90 **Di Trapani et al. (2020a)**, proposed the idea of three-strut fiber-section model, highlighting the  
91 importance of defining the inclination of the eccentric struts as a function of the geometrical and  
92 mechanical properties of the infilled frame. Despite this, no specific rules were given to define the  
93 inclination of the struts, and the predictive capacity of the model was tested only with a limited  
94 number of reference specimen tests, although with promising results.

95 Within this background, the paper formalizes the definition of a three-strut macro-element model  
96 based on the observation of the collapse mechanism of available experimental tests and refined  
97 numerical simulations of one-storey and multi-storey infilled frames. The model is defined using the  
98 *OpenSees* (**McKenna et al., 2000**) software platform. The major novelty is the definition of two  
99 parameters modulating the inclination of the struts and the resistance provided by the infill to the  
100 overall response. These parameters are easily evaluated through the analytical correlations provided  
101 in the paper, which put in relation the geometrical and mechanical characteristics of an infilled frame,  
102 with the geometric configuration and mechanical response of the equivalent strut model. In this way,  
103 the proposed model, can adapt its geometry and the stress-strain response of the struts to each infilled  
104 frame arrangement, providing a specialized simulation of the collapse mechanism. The  
105 aforementioned analytical correlation laws are obtained from an empirical dataset, specifically built  
106 by merging experimental pushdown test results and results from pushdown test simulation made with  
107 a refined finite element model. The validation of the model is carried against additional pushdown  
108 tests not previously considered for the definition of the dataset. A practical application of the proposed  
109 procedure is finally proposed for a six-storey building.

110

111

112

## 113 **Proposed macro-element model formulation**

114 The proposed modelling approach is based on the experimental observations of the damage mechanisms  
115 activating in single-storey and multi-storey infilled frames subject to pushdown tests. The model is  
116 implemented in OpenSees and is based on the adoption of distributed plasticity fiber-section elements  
117 for the RC frame. The model is easily reproducible with any finite element analysis program handling  
118 fiber-section elements. The experimental tests by **Li et al (2019)** and **Qian and Li (2017)** and the  
119 numerical investigations by **Di Trapani et al. (2020a)**, have clearly evidenced the behaviour of an  
120 infilled frame under progressive collapse conditions (**Fig. 1a-1b**), basically showing that:

- 121 • masonry portions enclosed at the corners undergoing a reduction of the original  $90^\circ$  angle in  
122 proximity of beam-column joints receive a confining action from the frame and because of  
123 this, undamaged corner regions form;
- 124 • confined masonry corner regions behave as rigid parts, inducing a migration of the position  
125 of the plastic hinges towards the inner part of the beam. In multi-storey infilled frames this  
126 occurs following a more or less linear pattern (**Fig. 1b, 2b**), so that for the external corner  
127 regions, the major movement of the plastic hinge position is observed at the highest floor  
128 (while no migration is observed at the lowest floor). This condition is inverted in  
129 correspondence of the internal corner regions. As a consequence of this, for the beams having  
130 intermediate position plastic hinges form in a position that can be approximately determined  
131 by intercepting the beam axis with the line joining the hinges at the upper and the lower floors  
132 (**Fig. 1b**).
- 133 • masonry at central zones undergoes significant damage due to diagonal compression. This  
134 induces sliding of bed joints and diagonal crushing in some cases.

135 A consequent schematization of the damage framework expected for building undergoing column  
136 losses is shown in **Fig. 2** for one-storey infilled frame buildings (**Fig. 2a**) and multi-storey infilled  
137 frame buildings (**Fig. 2b**). The major difference between these cases is related to the compression  
138 fields (depicted in blue in **Fig. 2**). In fact, as already mentioned, the masonry confined by the frame

139 is subjected to significant compression stresses making these parts of the infill working as  
140 compression struts. The latter have a unique slope which connects the positions of the plastic hinges  
141 forming at different places in the beams. This means that, in multi-storey infilled frames, the position  
142 of the plastic hinges depends on the storey level, while for the one-storey cases the damage  
143 configuration is fixed. The proposed model is conceived to reproduce the experimentally observed  
144 mechanical response of the single-storey and multi-storey infilled frames. The schematization of the  
145 model is proposed in **Fig. 3** for both the cases. The model is composed of 3 struts per each infilled  
146 frame. Struts S2 have infinite stiffness and strength and are used to effectively simulate the observed  
147 damage mechanism in which masonry at corners remains almost intact. The product  $\alpha_b l_b$  ( $\alpha_b < 1$ )  
148 represents the position of the connection node of the beam with the S2 strut. This consequently defines  
149 the angle of inclination of the struts and the location where the plastic hinge will form along the length  
150  $l_b$  because of the interaction with the infill. As it can be observed in **Fig. 3**, the distance  $\alpha_b l_b$  is defined  
151 once, both for the one-storey and multi-storey configurations, therefore the S2 struts of each infilled  
152 frame are parallel. For the multi-storey case, the connection points of S2 struts with the intermediate  
153 floor beams are obtained as the intersections of the straight lines connecting the origin points with the  
154 distances  $\alpha_b l_b$  at the top and bottom beams with the intermediate beams themselves. S2 struts at the  
155 different floors are therefore aligned. The parameter  $\alpha_b$  has a key role to the overall response, as it  
156 modulates the net length of the beams when the plasticization of the frame occurs. Therefore, high  
157 values of  $\alpha_b$  are associated with a major contribution of the frame to the overall strength, while on  
158 the contrary, low  $\alpha_b$  values induce minor frame resistance. More generally, the coefficient  $\alpha_b$   
159 considers the degree of coupling between the infill and the frame and therefore it defines the actual  
160 influence of the infill to the overall response of the frame. The definition of  $\alpha_b$  is therefore of crucial  
161 importance as it defines the geometry of the entire resisting mechanism (**Fig. 3**) although its definition  
162 depends on a quite large number of factors as it will be described in the subsequent sections.

163 The S1 strut models the shear behaviour of the infill in the inner part, which is subjected to diagonal  
 164 compression forces. The identification of S1 strut cross-section dimensions is performed starting from  
 165 the procedure proposed by **Di Trapani et al. (2018)** as modified in **Di Trapani et al. (2020a)**. The  
 166 thickness of the struts ( $t$ ) is the same as the actual thickness of the infill, the equivalent strut width ( $w$ )  
 167 is evaluated as:

$$168 \quad w = \frac{h_c}{l_b} \frac{c^*}{\lambda^{*\beta^*}} d \quad (1)$$

169 where, with respect to the original formulation, the effect of vertical loads on columns is ignored in  
 170 **Eq. (1)**, while the parameter  $\lambda^*$  is evaluated by means of the formula initially proposed by **Papia et**  
 171 **al. (2003)**, where the positions of  $l_b$  and  $h_b$  are inverted:

$$172 \quad \lambda^* = \frac{\tilde{E}_m}{E_c} \frac{t l_b'}{A_b} \left( \frac{l_b'^2}{h_c'^2} + \frac{1}{4} \frac{A_b}{A_c} \frac{h_c'}{l_b'} \right) \quad (2)$$

173 The symbols  $A_b$  and  $A_c$  represent the area of the cross-sections of beams and columns,  $E_c$  is the elastic  
 174 modulus of the concrete frame,  $\tilde{E}_m$  is the conventional elastic modulus taking into account both the  
 175 Young's moduli of masonry along the two orthogonal directions ( $E_{m1}$  and  $E_{m2}$ ) as:

$$176 \quad \tilde{E}_m = \sqrt{E_{m1} \cdot E_{m2}} \quad (3)$$

177 while the other symbols are deducible from **Fig. 3**. Parameters  $c^*$  and  $\beta^*$  are evaluated by the  
 178 following equations:

$$179 \quad \begin{aligned} c^* &= 0.249 - 0.0116\nu + 0.567\nu^2 \cong 0.254 \\ \beta^* &= 0.146 - 0.0073\nu + 0.126\nu^2 \cong 0.147 \end{aligned} \quad (4)$$

180 depending on Poisson's ratio ( $\nu$ ) of the infill along the diagonal direction. For the sake of simplicity,  
 181 the average Poisson's ratio can be used, otherwise the value  $\nu=0.1$  is assumed, providing the values  
 182 resulting in **Eq. (4)**. S1 struts are no-tension inelastic fiber-section trusses modelled with a  
 183 *Concrete02* material (parabolic with linear softening) available in *OpenSees*, defined by the four  
 184 parameters  $\tilde{f}_{md0}$  (peak-strength),  $\tilde{f}_{mdu}$  (ultimate-strength),  $\varepsilon_{md0}$  (peak-strain),  $\varepsilon_{mdu}$  (ultimate strain)



185 **(Fig. 4a)**. The equivalent strut is a phenomenological model which summarizes the complex response  
 186 of the infill as a function of the boundary condition (e.g. aspect ratio, masonry orthotropy, influence  
 187 of vertical stresses, frame-infill relative strength and stiffness). Therefore, the uniaxial stress-strain  
 188 response of S1 strut will not be coincident to the masonry nominal one but will be related to it by the  
 189 empirical relationships provided by **Di Trapani et al. (2018)**:

$$190 \quad f_{md0} = \tilde{f}_m \cdot 26.9 \cdot \alpha^{-0.28} \quad (5)$$

$$191 \quad f_{mdu} = f_{md0} \cdot (0.043 \cdot \beta - 0.06) \quad (6)$$

$$192 \quad \varepsilon_{md0} = \varepsilon_{m0} \cdot 3.024 \cdot \gamma^{0.347} \quad (7)$$

$$193 \quad \varepsilon_{mdu} = \varepsilon_{md0} \cdot 0.0184 \cdot \delta^{-1.166} \quad (8)$$

194 where, neglecting the influence of vertical loads on columns, and inverting the position of  $l_b$  and  $h_b$ ,  
 195 parameters  $\alpha$ ,  $\beta$ ,  $\gamma$  and  $\delta$  have the expressions:

$$196 \quad \alpha = \frac{\tilde{f}_m^2 \cdot w \cdot t}{f_{vm}^{0.2} (h_c / l_b) \cdot \lambda^{*0.2}} \quad (9)$$

$$197 \quad \beta = \frac{f_{md0}^{0.7} \cdot w \cdot t}{\tilde{E}_m^{0.2} d} \quad (10)$$

$$198 \quad \gamma = \left( \frac{f_{mdu}^2}{f_{md0}^2} \right) \left( \frac{E_c}{\tilde{E}_m^{1.5}} \right) \quad (11)$$

$$199 \quad \delta = \tilde{E}_m^{0.20} \cdot \varepsilon_{md0} \quad (12)$$

200 in which it is conventionally assumed  $\varepsilon_{m0} = 0.0015$  and  $\tilde{f}_m = \sqrt{f_{m1} \cdot f_{m2}}$ , is the conventional strength  
 201 of the masonry, which takes into account the strengths along the two orthogonal directions ( $f_{m1}$  and  
 202  $f_{m2}$ ). The peak and ultimate stresses  $\tilde{f}_{md0}$  and  $\tilde{f}_{mdu}$  are related with  $f_{md0}$  and  $f_{mdu}$  by a strength  
 203 reduction coefficient  $\xi$  ( $\leq 1$ ) taking into account a potential strength reduction associated with the  
 204 different expected failure modes for the infilled frame subjected to vertical loads (instead of  
 205 horizontal), as a function of the possible combination of geometric and mechanical characteristics of  
 206 the infilled-frame system, therefore :

207 
$$\begin{aligned}\tilde{f}_{md0} &= \xi \cdot f_{md0} \\ \tilde{f}_{mdu} &= \xi \cdot f_{mdu}\end{aligned}\tag{13}$$

208 The peak and ultimate strains are instead assumed as those evaluated by **Eqs. (7-8)** respectively.

209 Considering the above listed equations, the equivalent strut model is defined based on the two

210 parameters  $\alpha_b$  and  $\xi$ . Given the relevance that they assume on the overall response and the multitude

211 of variables on which they depend, the definition of  $\alpha_b$  and  $\xi$  is carried out using an empirical

212 approach rather than a mechanics-based one as described in the subsequent section.

213 As regards the reinforced concrete frame, this is modelled using distributed plasticity fiber-section

214 elements. A *Concrete02* model is used for confined core and unconfined cover concrete fibers (**Fig.**

215 **4b**). Confined ( $f_{cc0}, f_{ccu}, \varepsilon_{cc0}, \varepsilon_{ccu}$ ) and unconfined ( $f_{c0}, f_{cu}, \varepsilon_{c0}, \varepsilon_{cu}$ ) concrete parameters are evaluated

216 according to the model by **Razvi and Saatcoglu (1992)**. As regards rebars, given the large

217 displacements and damage achieved by the frame during the pushdown analyses, it was necessary to

218 include advanced material damage state. Rebars were modelled using the *Hysteretic* material

219 backbone curve in order to simulate fracture in tension, in correspondence of the ultimate stress-strain

220 capacity point ( $f_t, \varepsilon_{su}$ ), and buckling in compression (if any) in correspondence of the stress-strain

221 buckling point ( $\sigma^*, \varepsilon^*$ ) evaluated according to the **Dhokal and Maekawa (2002)** model. Finally, the

222 beam-columns intersection zones are modelled with rigid links. The definition of the rigid link

223 extensions can be alternatively carried out using ASCE/SEI 41-17 provisions.

224

## 225 **Framework and data-set for the empirical evaluation of coefficients $\alpha_b$ and $\xi$**

226 The determination of parameters  $\alpha_b$  and  $\xi$  is not easy to perform using a mechanical approach, in fact

227 this would require strong assumptions about specific collapse modes for the frame-infill system,

228 which are not simple to predict a-priori. The major unknown regards the masonry infill failure mode

229 which can alternatively be due to mortar joints sliding, diagonal cracking or mixed modes, and that

230 depends each time on the different combination of frame and infill mechanical and geometrical

231 properties and lateral constraint conditions. The procedure here followed, provides instead the

232 definition of two empirical correlations between the parameters  $\alpha_b$  and  $\xi$  and the geometrical and  
233 mechanical characteristics of the frame-infill system.

234 In order to derive the analytical correlation, a dataset of reference experimental and numerical  
235 pushdown tests has been defined. The tests were simulated in *OpenSees* using the proposed equivalent  
236 strut model. Parameters  $\alpha_b$  and  $\xi$  were initially assigned as trial values. The simulations were then  
237 repeated by iterating these parameter values up to the achievement of the best matching with the  
238 reference pushdown responses. The finally obtained values for  $\alpha_b$  and  $\xi$  parameters were then stored  
239 and associated with the geometrical and mechanical data of the respective infilled frame. The  
240 procedure was repeated for all the reference tests. Since the availability of experimental tests is limited,  
241 the robustness of the data-set was increased using the also the results from refined finite element  
242 simulations of pushdown tests carried out by **Di Trapani et al. 2020a**. The steps of the framework  
243 are below summarized:

- 244 1. Acquisition of experimental test data (geometric and materials data, pushdown curves);
- 245 2. Modeling of each experimental test with the proposed multi-strut model;
- 246 3. Iterative calibration of parameters  $\alpha_b$  and  $\xi$ ;
- 247 4. Acquisition of numerical test data from a refined, experimentally validated, FE model;
- 248 5. Modeling of each experimental test with the proposed multi-strut model;
- 249 6. Iterative calibration of parameters  $\alpha_b$  and  $\xi$ ;
- 250 7. Definition of two analytical correlation laws between the obtained parameters  $\alpha_b$  and  $\xi$  and the  
251 most representative geometrical and mechanical characteristics of the infilled frame;
- 252 8. Blind validation tests with experimental and FE specimens not included in the calibration phase.

253 A flow-chart of the framework is also illustrated in **Fig. 5**. The experimental tests used were those by  
254 **Qian and Li (2017)** (specimens WSS and WNL) and **Li et al. (2019)**. The formers are 1/4 scale two-  
255 storey reinforced concrete frames with brick masonry infills horizontally restrained from one-side  
256 only. The second is a 1/3 scale one-storey multi-bay reinforced concrete frames with brick masonry

257 infills. The test set-up did not provide lateral constraints, but the frame had one bay at each side of  
258 the central bays involved in the pushdown tests.

259 The numerical specimens were those by **Di Trapani et al. (2020a)**. The latter are full scale one-storey  
260 one-bay infilled frames having different aspect-ratios, lateral constraint degree (free or fixed), beam  
261 cross-section aspect ratio and reinforcement arrangement (seismic or non-seismic). These specimens  
262 have been modelled in the Atena 2D Version 5 (**Cervenka et al. 2017**) software platform, which is  
263 based on a smeared cracking formulation for concrete and also supports frictional interfaces to be  
264 used for modeling mortar joints. The typical assembly of the FE model is illustrated in **Fig. 6a**.  
265 Concrete frame elements and masonry blocks are modeled by using CCIsoQuad nonlinear finite  
266 elements. The constitutive model associated with concrete elements and masonry units having a  
267 failure surface (**Fig. 6b**). Mortar joints are simulated using 2D interfaces governed by a Mohr-  
268 Coulomb failure surface depending on friction coefficient ( $\mu$ ) and cohesion ( $c$ ) (**Fig. 6c**). The  
269 validation of the finite element modelling was performed by the authors in **Di Trapani et al. (2018)**.  
270 Details about the specimens and the test type are reported in **Table 1**. The identification the equivalent  
271 strut models is performed using **Eqs. (1-4)** for the determination of the S1 strut width and **Eqs. (5-**  
272 **12)** for the determination the nominal stress-strain response. Geometric and mechanical details of the  
273 experimental and numerical specimens together with the associated parameters identifying the  
274 equivalent struts are listed in **Tables 2-3**. Parameters  $\alpha_b$  and  $\xi$  are assigned as trial values in the first  
275 step. Before starting the iterative calibration of  $\alpha_b$  and  $\xi$ , the bare frame pushdown responses of the  
276 reference specimens and those provided by the models are compared. This preliminary comparison  
277 is carried out to check the reliability of the frame fiber-section model to reproduce the bare frame  
278 response, so that the subsequent calibration of parameters  $\alpha_b$  and  $\xi$  will not be affected by a  
279 compensation of predictive errors of the frame model. For the sake of space only three sample  
280 comparisons between the bare frame reference specimens' responses and the bare frame model  
281 predictions are shown in **Figs. 7**. The latter confirm the reliability of the frame model in reproducing  
282 the pushdown tests.

283 Numerical simulation of the infilled frames pushdown tests is then carried out. Parameters calibration  
284 process is performed by comparing the reference pushdown responses and the model predictions  
285 iteratively varying parameters  $\alpha_b$  and  $\xi$  to get the best matching of the curves. The basic matching  
286 criterion followed was an energetic criterion, that is the minimization of the difference between the  
287 areas below the reference pushdown curve of the specimen  $A_{exp}$  and the predicted one  $A_{pred}$ , so that  
288  $|A_{exp} - A_{pred}|$  is minimized. The adequacy of the results obtained by this approach was finally checked  
289 by the authors at the end of each test. The ranges of variation assumed were 0.15-0.5 for  $\alpha_b$  and 0.25-  
290 1.0 for  $\xi$ . Results at the end of the calibration process are shown in **Fig. 8-9**, where numerical  
291 predictions and reference pushdown curves are depicted. It can be generally observed that, despite  
292 the large geometric and mechanical nonlinearity achieved during the tests, an adequate calibration of  
293  $\alpha_b$  and  $\xi$  allowed a sufficiently accurate prediction of the overall pushdown response, giving a  
294 positive feedback on the reliability of the proposed modelling approach. Some comparisons between  
295 the deformed shapes of the experimental and numerical specimens and those of the multi-strut models  
296 are shown in **Fig. 10**, demonstrating the consistency of the actual damage mechanisms with the  
297 predicted ones. Optimal results obtained for parameters  $\alpha_b$  and  $\xi$  at the end of the calibration process  
298 of each specimen are finally listed in **Table 4**, together with the dimensional parameters resulting by  
299 their application. As regards  $\alpha_b$ , the values range between 0.15 and 0.50, meaning that the plastic  
300 hinges in beams can form in a region comprised between 15% and 50% of the internal length  $l_b$ . This  
301 is definitely consistent with the experimental and numerical evidence from the considered specimens  
302 (**Fig. 10**). Regarding  $\xi$  values, the range is 25%-100% of the diagonal resistance  $f_{md0}$ . This wide range  
303 should not be surprising, but highlights the fact that the infill contribution to the overall resistance is  
304 extremely variable and depends on the resistance associated with the actual failure mechanism  
305 developing, as well described in the following section.

306

307

## 308 **Empirical correlation laws for $\alpha_b$ and $\xi$**

309 The experimental and numerical data-sets containing the calibrated parameters  $\alpha_b$  and  $\xi$  together with  
310 the associated geometrical and mechanical features of the respective infilled frames are merged into  
311 a unique hybrid data-set. Results are then analyzed in order to understand the dependence of these  
312 parameters in a more general framework. An interpretation of the obtained  $\alpha_b$  and  $\xi$  values can be  
313 given by recognizing the actual role of these parameters to the overall response. In fact, while  $\xi$   
314 modulates the contribution of the infill in terms of strength,  $\alpha_b$  modulates the shape of the collapse e  
315 mechanism, namely the amplitude of the intact portion of masonry enclosed at the corners.  
316 Consequently,  $\alpha_b$  has effect on the vertical strength of the frame, as it defines the net shear span of  
317 the beams involved in the collapse mechanism (**Fig. 11**). The modulation by means of coefficients  $\alpha_b$   
318 and  $\xi$  allows considering the reciprocal influence of the frame to the final resistance of the infill and,  
319 vice versa, the influence of the infill to the final resisting mechanism of the frame. Consistently with  
320 this consideration, it can be observed the lowest  $\xi$  values are associated with specimens having  
321 reduced strength and stiffness of the frame with respect to that of the infill, so that a lower confining  
322 action is exerted and a sliding failure mode is more likely. On the contrary, a stronger confining action  
323 by a stiffer frame, will orient failure to a crushing mode which is typically associated with a larger  
324 strength. At the same time, the coefficient  $\alpha_b$  has shown to be more influenced by the strength ratio  
325 between the frame and the infill, therefore the lower  $\alpha_b$  values have been obtained for the frames  
326 having low strength with respect to the infill strength.

327 In this framework a crucial role is exerted by the lateral constraint degree, which influences the  
328 vertical stiffness of the frame and even more its strength. In fact, in the case of rigid or semi-rigid  
329 lateral contains, the axial force reaction to the pushing action of beams after the first cracking is  
330 relevant and significantly increases the resisting end moments ( $M_p^+$ ,  $M_p^-$ ). On the other hand, more  
331 effective lateral constraint degree increases the frame stiffness and the associated confining action to

332 the infill with major exploitation of the infill strength. The scheme of the typical collapse mechanism  
 333 is depicted in **Fig. 11** for the one-storey infilled frame.

334 Based on the aforementioned assumptions, the best correlation between  $\xi$  and the geometric and  
 335 mechanical properties of the frame-infill system is found with the parameter  $\kappa$  so defined:

$$336 \quad \kappa = \frac{K_f}{K_s} \sqrt{\frac{l_b}{h_c}} \sqrt{\frac{\tilde{f}_m}{f_{vm}}} \quad (14)$$

337 where  $K_f$  is the conventional vertical stiffness of the frame obtained as the sum of the shear stiffnesses  
 338 of the  $n_b$  beams involved in the mechanism:

$$339 \quad K_f = \sum_{i=1}^{n_b} \psi_i \cdot \frac{E_{ci} I_{bi}}{l_{bi}^3} \quad (15)$$

340 and  $K_s$  is the conventional vertical stiffness contribution provided by the  $n_s$  infills involved in the  
 341 mechanism at all the stories:

$$342 \quad K_s = \sum_{j=1}^{n_s} \lambda_j \frac{\tilde{E}_{mj} \cdot t_j \cdot w_j}{d_j} \cdot \sin \theta_j \quad (16)$$

343 In the previous equation  $i=1 \dots n_b$  is an index referred to the generic beam and  $j=1 \dots n_s$  is an index  
 344 referred to the generic strut. The coefficients  $\psi_i$  and  $\lambda_j$  are used to consider the influence of the lateral  
 345 constraint degree on the real stiffness of the beams and of the struts. The following boundary values  
 346 are assumed depending on the type of constraint:

$$347 \quad \psi_i = \begin{cases} 12 & \text{(rigid)} \\ 6 & \text{(free)} \end{cases} \quad \lambda_j = \begin{cases} 1 & \text{(rigid)} \\ 0.5 & \text{(free)} \end{cases} \quad (17)$$

348 In **Eq. (16)**,  $\theta_j$  is the angle of inclination of the S1 strut. For the one storey infilled frame this is  
 349 depending only on the geometry of the frame, while in the case of a multi-storey infilled frame, this  
 350 depending on  $\alpha_b$  (**Fig. 3b**) which is still depending on  $\theta_j$ . The determination of  $\theta_j$  can be thus  
 351 performed iteratively, or in a simpler way, this can be assumed as the average between the maximum  
 352 and minimum slopes ( $\theta_{max}$  and  $\theta_{min}$  respectively) resulting by assuming  $\alpha_b = 0.5$  and  $\alpha_b = 0.15$  (**Fig.**  
 353 **12**):

354 
$$\theta_j = \frac{\theta_{max} + \theta_{min}}{2} \quad (18)$$

355 where supposing that all the stories have the same interstorey height ( $h_c'$ ), it can be easily found:

356 
$$\theta_{max} = \arctan\left(\frac{nh_c'}{nl_b' - (n-1)(0.5l_b + 0.5h_{wc})}\right); \theta_{min} = \arctan\left(\frac{nh_c'}{nl_b' - (n-1)(0.15l_b + 0.5h_{wc})}\right) \quad (19)$$

357  
 358 Resulting values of  $K_f$ ,  $K_s$  and  $\kappa$  for the different specimens are reported in **Table 5**. The best  
 359 correlation between  $\xi$  and  $\kappa$ , fitting experimental and numerical data can be established by the  
 360 following exponential correlation law (**Fig. 13a**):

361 
$$\xi = 0.212 \cdot e^{1.45\kappa} \quad (R^2 = 0.89) \quad (20)$$

362 which results in a determination coefficient of 0.89. The values of  $\xi$  resulting from **Eq. (20)** can be  
 363 reasonably assumed in the range  $0.25 \leq \xi \leq 1.0$ .

364 The correlation of the parameter  $\alpha_b$  with the characteristics of the infilled frame can be expressed as  
 365 a function of the frame-infill strength ratio  $\rho$ , defined as:

366 
$$\rho = \frac{R_f}{R_s} \quad (21)$$

367 in which  $R_f$  is the conventional vertical strength of the frame, obtained as:

368 
$$R_f = \sum_{i=1}^{n_{Mp}} \frac{M_{p,i}^- + M_{p,i}^+}{l_b} \quad (22)$$

369 where, with reference to the simplified limit equilibrium scheme of the generic double span in **Fig.**  
 370 **14a**, the subscripts  $i$  denotes the generic plastic negative and positive moments at the ends of each  
 371 beam involved in the collapse mechanism,  $n_{Mp}$  is the number of end cross-section where the plastic  
 372 moments form, while  $l_b$  is the net span length. The plastic moments have positive sign and are  
 373 evaluated considering the maximum axial forces acting on the beams during the pushdown analysis  
 374 ( $N_{b,max}$ ).  $R_s$  is the conventional vertical resistance provided by the infills, obtained considering the  
 375 limit equilibrium of the hinged simplified scheme of the generic storey in **Fig. 14b** as:



376

$$R_s = \sum_{j=1}^{n_s} \tilde{f}_{mdo,j} \cdot t_j \cdot w_j \cdot \sin \theta_j \quad (23)$$

377

378

where the subscript  $j$  denotes the terms related to the generic S1 strut involved in the collapse mechanism. For the correlation between  $\rho$  and  $\alpha_b$  two possible expressions are provided (**Fig. 13b**):

379

$$\alpha_b = -0.09\rho^3 + 0.54\rho^2 - 1.05\rho + 0.86 \quad (R^2 = 0.93) \quad (24)$$

380

$$\alpha_b = 0.28\rho^{-0.58} \quad (R^2 = 0.87) \quad (25)$$

381

382

383

384

385

386

387

388

389

390

391

392

393

394

395

396

397

398

399

400

The two expressions have similar determination coefficients (0.93 and 0.87 respectively) and can be used alternatively or to get an average value for  $\alpha_b$ . Consistently with the actual experimental and numerical observations, the values of  $\xi$  resulting from **Eqs. (24-25)** can assumed be in the range  $0.15 \leq \alpha_b \leq 0.5$ . Resulting values of  $R_f$ ,  $R_s$ ,  $\rho$  and  $N_{b,max}$  for the different specimens are reported in **Table 5**. It is noteworthy observing that the determination of the strength of the frame ( $R_f$ ), and therefore of the coefficient  $\rho$ , is subject to the evaluation plastic moments at the ends of the beams, which in turn are depending on the maximum axial forces ( $N_{b,max}$ ) developing because of the pushing action of the beams on the lateral supports. The latter are not straightforward to evaluate in practice, since they vary at each step of the pushdown analysis, therefore, in order to use **Eq. (22)**, two strategies can be adopted. The first is running a pushdown analysis supposing a trial value of  $\alpha_b$  to get an estimation of the maximum axial forces acting on beams. The second is using the analytical correlation laws defined as described in the following.

The maximum compression axial force achieved by the beams in a pushdown tests basically depends on two factors. One is the lateral constraint degree, the more the constraints are stiff, the more the axial lateral reaction increases and so the axial force. The second is the beam height-to-length ratio ( $\chi=h_{wb}/l_b$ ), as this conditions to the arching action developed by the beams after the first cracking. This is clear from **Fig. 15a**, which shows the distribution of maximum dimensionless axial forces ( $v_{b,max}=N_{b,max} / f_c b_{wb} h_{wb}$ ) recorded for the previously analyzed experimental and numerical specimens as a function of  $\chi$  and the lateral restraint conditions. In **Fig. 15b**, the trend of the average

401 dimensionless axial forces in beams is reported as a function of the vertical displacement and for the  
402 different constraint conditions.

403 It is found that the two following simple polynomial correlation can be defined between  $v_{b,max}$  and  $\chi$   
404 for the two cases of rigid and free lateral constraints:

$$405 \quad v_{b,max} = \begin{cases} -8.27\chi^2 + 2.74\chi + 0.017 & \text{(rigid)} \\ -5.79\chi^2 + 1.36\chi - 0.041 & \text{(free and rigid-free)} \end{cases} \quad (26)$$

406 As previously mentioned, expressions in **Eq. (25)** can be used as a simple way to predict the  
407 maximum axial force acting on the beams and therefore estimating the associated plastic moments to  
408 introduce in **Eq. (22)**. An interpolation between the two functions can be used to estimate  $v_{b,max}$  the  
409 cases having semi-rigid connections.

410

#### 411 **Blind validation tests**

412 Based on the obtained formulation, the procedure for the complete analytical definition of the  
413 proposed infilled frame multi-strut model follows the below reported steps:

- 414 1. Evaluation of the equivalent strut width  $w$  (**Eqs. 1-4**);
- 415 2. Evaluation of the nominal stress-strain parameters of S1 strut ( $f_{md0}, f_{mdu}, \varepsilon_{md0}, \varepsilon_{mdu}$ ) (**Eqs. 5-12**);
- 416 3. Determination of  $\xi$  (**Eqs. 14-20**);
- 417 4. Determination of  $\tilde{f}_{md0}$  and  $\tilde{f}_{mdu}$  (**Eqs. 13**);
- 418 5. Determination of  $\alpha_b$  (**Eqs. 21-26**);

419 This procedure has been validated by applying it for the simulation of four reference tests not  
420 belonging to previously defined data-set used to build the empirical correlations. The specimens  
421 consisted of one experimental test by **Qian and Li (2017)** (Specimen WNS) and three numerical tests  
422 of the refined FE models by **Di Trapani et al (2020a)** Details about the specimens and the test types  
423 are reported in **Table 6**, while **Tables 7-8** collect all the fundamental geometric and mechanical data  
424 for the definition of the equivalent strut and the nominal stress-strain parameters. Parameters  $\kappa$  and

425  $\rho$ , evaluated according to **Eqs. (14)** and **(21)** are reported in **Table 9**, together with the dimensionless  
426 axial forces ( $v_{b,max}$ ) estimated by **Eq. (26)**. Parameters  $\alpha_b$  and  $\xi$  finally resulting are reported in **Table**  
427 **10**. The comparison between experimental force-displacement curves and numerical predictions are  
428 depicted in **Fig. 16**. It can be observed that for all the considered cases, numerical predictions resulted  
429 in a very good agreement with the test data, providing a sufficiently reliable prediction of the peak  
430 resisting capacity and the post-peak branch, despite the large uncertainty associated with the advanced  
431 damage state of materials during the tests. This result is also confirmed by the consistency between  
432 actual and predicted deformed shapes as illustrated in **Fig. 17**.

#### 433 434 **Application of the proposed method to a case-study structure**

435 The proposed modelling methodology is applied to perform the progressive collapse analysis of  
436 infilled frames case-study structure. A multi-bay, six-stories infilled frame reinforced concrete  
437 structure (**Fig. 18**) is used as example. The structure is supposed undergoing the central columns loss.  
438 The frame is constituted by concrete having compressive strength  $f_c=25$  MPa and steel rebars with  
439 yielding stress  $f_y=450$  MPa. The structure is designed according to the Italian design regulation (NTC  
440 2018). Geometric and mechanical details of the frame and of the infills are reported in **Table 11**.  
441 Detail of reinforcement of the central spans are illustrated in **Table 12**. As regards the infills outside  
442 the progressive collapse mechanism, these are modelled with a standard equivalent strut model (e.g.  
443 **Di Trapani et al., 2018**). A semi-rigid lateral constrain degree is assumed for the first five stories,  
444 while for the last storey the constraint degree is supposed as free. The structure is subjected to a  
445 pushdown tests, comparing the results with those obtained supposing the bare frame configuration in  
446 the central bays. The detailed calculation steps are exposed in Appendix. The resulting geometry for  
447 the equivalent strut model is illustrated in **Fig. 19**.  
448 Results of the pushdown tests are shown in **Fig. 20a**. The latter show a strength increment of +40%  
449 for the model having the infills in the central bays and noticeable stiffness increase. The post-peak

450 behaviour is, as expected, characterized by a rapid strength loss associated with the failure of the  
451 infills. On the contrary, the model with bare central spans shows a more ductile behaviour up to a  
452 displacement of 200 mm followed by a rapid strength loss. The two models show similar residual  
453 resistance in the last stages of the test. A test of the adequacy of the hypothesis of considering a semi-  
454 rigid behaviour of lateral constrains by **Eq. (25)** has been also carried out. **Fig. 20b** shows a good  
455 agreement between the average maximum value of the dimensionless axial force predicted by **Eqs**  
456 **(25)** and the actual dimensionless axial force trend during the analysis. The deformed shapes at the  
457 same vertical displacement (300 mm) of the two models are finally shown in **Fig. 21**.

458  
459

## Conclusions

460 The simulation of progressive collapse response of frame structures due to accidental column losses  
461 is complicated because of the high mechanic and geometric nonlinearity. The complexity of the  
462 collapse mechanism is accentuated by the influence of masonry infills which significantly interact  
463 with primary RC structures. From the observation of experimental and numerical pushdown tests it  
464 is evident that the infill-frame interaction induce: a) a migration of the plastic hinges towards the  
465 inner part of the beams; b) the formation of regions without damage for the masonry portions enclosed  
466 at the corners because of the confining action exerted by the frame in the collapsed central column  
467 configuration; b) the sliding of bed-joints or diagonal crushing in the central zones of the infills.  
468 These mechanisms can influence in a more or less relevant way the overall resistance, and this  
469 depends each time on the coupling between the frame and the infill.

470 The paper presented a simplified multi-strut macro-model to be used for progressive collapse  
471 simulations. The major novelty is just the capability of the model to adapt its geometry and  
472 mechanical properties of the struts as a function the characteristics of the infilled frame, to match as  
473 much as possible the mechanisms above described. The model provides different definition of the  
474 geometry in the case of multi-storey frames. The definition of the model is regulated by two  
475 fundamental parameters,  $\alpha_b$  and  $\xi$ , modulating the slope of the external struts and the stress-strain of

476 the central strut respectively. These parameters can be evaluated by the analytical correlations  
477 provided in the paper and basically depend on the strength and stiffness ratios between the frame and  
478 the infill. The analytical correlations have been obtained from an empirical hybrid dataset, defined by  
479 merging test data from real experimental tests and refined numerical simulations. The validation of  
480 the model, carried out against four external blind tests, gave confirmation of a sufficient predictive  
481 reliability of the model, even in consideration of the significant uncertainties affecting the response  
482 of infilled frame systems. Concluding, the proposed model results a flexible and computationally  
483 effective instrument to be used for the design and the assessment of robustness of new and existing  
484 reinforced concrete infilled frames. Considering the noticeable influence of the infills to the overall  
485 progressive collapse response, future works could exploit this modelling methodology to investigate  
486 and compare the progressive collapse responses of bare and infilled frames under dynamic regime.

487  
488

## APPENDIX – Details of calculations for the sample structure

489 With reference to the geometric and material details reported in **Table 11** for the sample structure,  
490 the definition of the multi-strut model provides the following calculation steps:

491 1. Calculate  $\lambda^*, c^*, \beta^*, w$  for S1 strut

$$\lambda^* = \frac{\tilde{E}_m}{E_c} \frac{t l_b'}{A_b} \left( \frac{l_b'^2}{h_c'^2} + \frac{1}{4} \frac{A_b}{A_c} \frac{h_c'}{l_b'} \right) = \frac{5675}{31476} \frac{300 \times 6300}{150000} \left( \frac{6300^2}{3400^2} + \frac{1}{4} \frac{150000}{320000} \frac{3400}{6300} \right) = 7.94 \quad (27)$$

$$c^* \cong 0.254; \quad \beta^* \cong 0.147 \quad (28)$$

$$w = \frac{h_c}{l_b} \frac{c^*}{\lambda^* \beta^*} d = \frac{2900}{5500} \frac{0.254}{7.94^{0.147}} 7159 = 707 \text{ mm} \quad (29)$$

492 2. Calculate the nominal stress-strain parameters for S1 strut  $f_{md0}, f_{mdu}, \varepsilon_{md0}, \varepsilon_{mdu}$  (**Eqs. 5-12**)::

$$\alpha = \frac{\tilde{f}_m^2 \cdot w \cdot t}{f_{vm}^{0.2} (h_c / l_b) \cdot \lambda^{*0.2}} = \frac{6.02^2 \times 707 \times 300}{1.07^{0.2} (2900 / 5500) 7.94^{0.2}} = 9.50 \times 10^6 \quad (30)$$

$$\beta = \frac{f_{md0}^{0.7} \cdot w \cdot t}{\tilde{E}_m^{0.2} d} = \frac{1.61^{0.7} \times 707 \times 300}{5675^{0.2} 7159} = 7.34 \quad (31)$$

$$\gamma = \left( \frac{f_{mdu}^2}{f_{md0}} \right) \left( \frac{E_c}{\tilde{E}_m^{1.5}} \right) = \left( \frac{0.41^2}{1.61} \right) \left( \frac{31476}{5675^{1.5}} \right) = 0.00772 \quad (32)$$

$$\delta = \tilde{E}_m^{0.20} \cdot \varepsilon_{md0} = 5675^{0.20} \times 0.000839 = 0.00473 \quad (33)$$

$$f_{md0} = \tilde{f}_m \cdot 26.9 \cdot \alpha^{-0.287} = 6.02 \times 26.9 \times (9.50 \times 10^6)^{-0.287} = 1.61 \text{ MPa} \quad (34)$$

$$f_{mdu} = f_{md0} (0.043 \cdot \beta - 0.06) = 1.61 (0.043 \times 7.34 - 0.06) = 0.41 \text{ MPa} \quad (35)$$

$$\varepsilon_{md0} = \varepsilon_{m0} \cdot 3.024 \cdot \gamma^{0.347} = 0.0015 \times 3.024 \times 0.00772^{0.347} = 0.000839 \quad (36)$$

$$\varepsilon_{mdu} = \varepsilon_{md0} \cdot 0.0184 \cdot \delta^{-1.166} = 0.000839 \cdot 0.0184 \cdot 0.00473^{-1.166} = 0.00794 \quad (37)$$

493 3. Calculate  $\xi$  (Eqs. 14-20)

494

$$\begin{aligned} \theta_{\min} &= \arctan \left( \frac{nh'_c}{nl'_b - (n-1)(0.15l_b + 0.5h_{wc})} \right) = \\ &= \arctan \left( \frac{5 \times 3400}{5 \times 6300 - 4(0.15 \times 5500 + 0.5 \times 800)} \right) = 32.6^\circ \end{aligned} \quad (38)$$

$$\begin{aligned} \theta_{\max} &= \arctan \left( \frac{nh'_c}{nl'_b - (n-1)(0.5l_b + 0.5h_{wc})} \right) = \\ &= \arctan \left( \frac{5 \times 3400}{5 \times 6300 - 4(0.5 \times 5500 + 0.5 \times 800)} \right) = 42.0^\circ \end{aligned} \quad (39)$$

$$\theta_j = \frac{\theta_{\min} + \theta_{\max}}{2} = \frac{32.6^\circ + 42.0^\circ}{2} = 37.3^\circ \quad (40)$$

495 The beams belonging to the first five spans are considered having a semi-rigid lateral constrains at

496 the ends ( $\psi_i=9, \lambda_j=0.75$ ). The beams belonging to the last span are considered having no lateral

497 constrains ( $\psi_i=6, \lambda_j=0.75$ ). Therefore:

$$K_f = \sum_{i=1}^{n_b} \psi_i \cdot \frac{E_c I_{bi}}{l_{bi}^3} = (9 \times 10 + 6 \times 2) \times \frac{31476 \times 3125000000}{5500^3} = 60303 \text{ kN} / \text{m} \quad (41)$$

$$K_s = \sum_{j=1}^{n_s} \lambda_j \frac{\tilde{E}_{mj} \cdot t_j \cdot w_j}{d_j} \cdot \sin \theta_j = (0.75 \times 8 + 0.5 \times 2) \times \frac{5675 \times 300 \times 707}{7159} \sin(37.3^\circ) = 713208 \text{ kN} / \text{m} \quad (42)$$

$$\kappa = \frac{K_f}{K_s} \sqrt{\frac{l_b}{h_b}} \sqrt{\frac{\tilde{f}_m}{f_{vm}}} = \frac{60303}{713208} \sqrt{\frac{5500}{2900}} \sqrt{\frac{6.02}{1.07}} = 0.28 \quad (43)$$

$$\xi = 0.212 \cdot e^{1.45\kappa} = 0.212 \cdot e^{1.45 \times 0.28} = 0.32 \quad (44)$$

498 4. Calculate  $\tilde{f}_{md0}$  and  $\tilde{f}_{mdu}$  (**Eqs. 13**):

$$\tilde{f}_{md0} = \xi \cdot f_{md0} = 0.32 \times 1.61 = 0.51 \text{ MPa} \quad (45)$$

$$\tilde{f}_{mdu} = \xi \cdot f_{mdu} = 0.32 \times 0.41 = 0.13 \text{ MPa} \quad (46)$$

499 5. Calculate  $\alpha_b$  (**Eqs. 21-26**):

$$\chi = \frac{h_{wb}}{l_b} = \frac{500}{5500} = 0.091 \quad (47)$$

500 Consistently with the previous assumptions the dimensionless axial forces of the beams belonging to  
 501 the first five spans are evaluated as average ( $v_{b,max(semi-rigid)}$ ) between the values obtained from the two  
 502 expressions in **Eq. (26)**. The second expression in **Eq. (26)** is used for the top beams ( $v_{b,max(free)}$ ).

$$v_{b,max(rigid)} = -8.27\chi^2 + 2.74\chi + 0.02 = -8.27 \times 0.091^2 + 2.74 \times 0.091 + 0.02 = 0.20 \quad (48)$$

$$v_{b,max(free)} = -5.79\chi^2 + 1.36\chi - 0.04 = -5.79 \times 0.091^2 + 1.36 \times 0.091 - 0.04 = 0.036 \quad (49)$$

$$v_{b,max(semi-rigid)} = v_{b,max(rigid)} + v_{b,max(free)} = \frac{0.20 + 0.036}{2} = 0.12 \quad (50)$$

503 The resulting axial forces used to evaluate the plastic end moments of the beams are then:

504

$$N_{b,max(semi-rigid)} = v_{b,max(semi-rigid)} f_c h_{wb} b_{wb} = 0.12 \times 25 \times 500 \times 300 = 450000 \text{ N} = 450 \text{ kN} \quad (51)$$

$$N_{b,max(free)} = v_{b,max(free)} f_c h_{wb} b_{wb} = 0.036 \times 25 \times 500 \times 300 = 135000 \text{ N} = 135 \text{ kN} \quad (52)$$

It follows:

$$R_f = \sum_{i=1}^{n_{M_p}} \frac{M_{p,i}^-}{l_b} + \sum_{i=1}^{n_{M_p}} \frac{M_{p,i}^+}{l_b} = 2 \left( \frac{368.5 + 368.5 + 368.5 + 327.8 + 327.8 + 273.3}{5.5} \right) + \quad (53)$$

$$+ 2 \left( \frac{265.2 + 265.2 + 265.2 + 224.6 + 224.6 + 154.7}{5.5} \right) = 1249 \text{ kN}$$

$$R_s = \sum_{j=1}^{n_s} \tilde{f}_{mdo,j} \cdot t_j \cdot w_j \cdot \sin \theta_j = 10 \times 0.51 \times 300 \times 707 \times \sin(37.3^\circ) = 655503 \text{ N} = 655.5 \text{ kN} \quad (54)$$

$$\rho = \frac{R_f}{R_s} = \frac{1249}{655.5} = 1.90 \quad (55)$$

Calculation of  $\alpha_b$  using **Eq. (24)**

$$\alpha_b = -0.09\rho^3 + 0.54\rho^2 - 1.05\rho + 0.86 = -0.09 \times 1.90^3 + 0.54 \times 1.90^2 - 1.05 \times 1.90 + 0.86 = 0.20 \quad (56)$$

$$\alpha_b l_b = 0.20 \times 5500 = 1100 \text{ mm} \quad (57)$$

Alternative calculation of  $\alpha_b$  using **Eq. (25)**

$$\alpha_b = 0.28\rho^{-0.58} = 0.28 \cdot 1.90^{-0.58} = 0.19 \quad (58)$$

505

## Data Availability Statement

506

Some or all data, models, or code generated or used during the study are available from the

507

corresponding author by request. (OpenSees models).

508

## References

509

Adam, J.M., Parisi, F., Sagasetac, J., Lu, X. 2018. "Research and practice on progressive collapse and robustness of building structures in the 21st century." *Eng. Struct.* 173: 122–149.

510

511

Caliò, I., Pantò, B. 2014. "A macro-element modelling approach of Infilled Frame Structures." *Computers & Structures* 143:91–107.

512

513

Calvi, G.M., Bolognini, D. 2001. "Seismic response of reinforced concrete frames infilled with weakly reinforced masonry panels." *J. Earthq. Eng.* 5(02):153–85.

514

515

Cervenka, J., L. Jendele, and V. Cervenka. 2017. ATENA program documentation. Praha 5, Czech Republic: Cervenka Consulting.

516

517

Colangelo, F. 2005 "Pseudo-dynamic seismic response of reinforced concrete frames infilled with non-structural brick masonry." *Earthquake Eng Struct Dyn* 34: 1219–1241.

518

519

Crisafulli, F.J., Carr, A.J. 2007. "Proposed macro-model for the analysis of infilled frame structures." *Bull N Z Soc Earth. Eng.* 40(2):69–77.

520

521

Dhakal, R.P., Maekawa, K. 2002. "Modeling for Postyield Buckling of Reinforcement." *J. Struct. Eng.* 128(9): 1139-1147.

522

523

Di Trapani, F., Bertagnoli, G., Ferrotto, M.F., Gino, D. 2018. "Empirical equations for the direct definition of stress-strain laws for fiber-section based macro-modeling of infilled frames." *J. Eng. Mech.* 144(11): 04018101.

524

525

526

Di Trapani, F., Giordano, L., Mancini, G. 2020-a. "Progressive Collapse Response of Reinforced Concrete Frame Structures with Masonry Infills." *J. Eng. Mech.* 146(3): 04020002

527

528

Di Trapani F., Bolis V., Basone F., Preti M. 2020-b. "Seismic reliability and loss assessment of RC frame structures with traditional and innovative masonry infills." *Eng. Struct.* 208:110306.

529

530

El-Dakhkhni, W., Elgaaly, M., Hamid, A. 2003. Three-Strut model for concrete masonry infilled steel frames. *J. Struct. Eng.* 129(2):177–85.

531

532

Farazman, S., Izzuddin, B.A, Cormie, D. 2013. "Influence of Unreinforced Masonry Infill Panels on the Robustness of Multistory Buildings." *J. Perform. Constr. Facil.* 27(6): 673-682.

533



- 534 Furtado, A., Rodrigues, H., Arêde, A., Varum, H. 2015. "Simplified macro-model for infill masonry  
535 walls considering the out-of-plane behaviour." *Earthquake engineering and structural dynamics*  
536 45(4): 507-524.
- 537 Izzuddin, B.A., Vlassis, A. G., Elghazlouli, A. Y., Nethercot, D.A. 2008. "Progressive collapse of  
538 multi-storey buildings due to sudden column loss. Part I: Simplified assessment framework." *Eng.*  
539 *Struct.* 30(5): 1308–1318.
- 540 Kakaletsis, D. J., and C. G. Karayannis. 2009. "Experimental investigation of infilled reinforced  
541 concrete frames with openings." *ACI Struct. J.* 102 (2): 132–141.
- 542 Kunnath, S.K., Bao, Y., El-Tawil, S. 2018. "Advances in Computational Simulation of Gravity-  
543 Induced Disproportionate Collapse of RC Frame Buildings." *J. Struct. Eng.* 144(2): 03117003.
- 544 Li, S., Kose, M.M., Shan, S., Sezen H. 2019. "Modeling Methods for Collapse Analysis of Reinforced  
545 Concrete Frames with Infill Walls." *J. Struct. Eng.* 145(4): 04019011.
- 546 Marchand, K.A., Stevens, D.J. 2015. "Progressive Collapse Criteria and Design Approaches  
547 Improvement." *J. Perform. Constr. Facil.* 29(5): B4015004.
- 548 McKenna F., Fenves G.L., Scott M.H. 2000. Open system for earthquake engineering simulation.  
549 University of California, Berkeley, CA.
- 550 Mehrabi, A.B., Shing, P.B. 1997. "Finite element modelling of masonry-infilled RC frames." *J.*  
551 *Struct. Eng.* 123(5): 604-13.
- 552 Mehrabi, A.B., Shing, P.B., Schuller, M.P., Noland, L. 1996. "Experimental Evaluation of Masonry-  
553 Infilled RC Frames." *J. Struct. Eng.* 122(3): 228-237.
- 554 Morandi, P., Hak, S., Magenes, G. 2018. "In-plane Experimental Response of Strong Masonry  
555 Infills." *Eng. Struct.* 156: 503-521.
- 556 Panagiotakos, T.B., Fardis, M.N. 1996. "Seismic response of infilled RC frames structures." XXI  
557 WCEE, Acapulco, Mexico.
- 558 Papia, M., Cavaleri, L., Fossetti, M. 2003. "Infilled frames: developments in the evaluation of the  
559 stiffening effect of infills." *Structural engineering and mechanics* 16(6): 675-93.
- 560 Pham X.D., Tan K.H., Yu J. 2015. "A simplified approach to assess progressive collapse resistance."  
561 *Eng. Struct.* 101: 45-57
- 562 Pham, A.T., Tan, K.H., Yu, J. 2017. "Numerical investigations on static and dynamic responses of  
563 reinforced concrete sub-assemblages under progressive collapse." *Eng. Struct.* 149: 2–20.
- 564 Qian, K. & Li, B. 2017. "Effects of Masonry Infill Wall on the Performance of RC Frames to Resist  
565 Progressive Collapse." *J. Struct. Eng.* 143(9): 04017118.
- 566 Ren, P., Li, Y., Lu, X., Guan, H., Zhou, Y. 2016. "Experimental investigation of progressive collapse  
567 resistance of one-way reinforced concrete beam–slab substructures under middle-column-  
568 removal scenario" *Eng. Struct.* 118: 28–40
- 569 Razvi S.R., Saatcioglu M. 1992. "Strength and Ductility of Confined Concrete." *J. Struct. Eng.*  
570 118(6): 1590-1607.
- 571 Shan, S. D., Li S., Xu S. Y., Xie L. L. 2016. "Experimental study on the progressive collapse  
572 performance of RC frames with infill walls." *Eng. Struct.* 111: 80–92.
- 573 Stavridis, A., Shing, P.B. 2010. "Finite-Element Modeling of Nonlinear Behavior of Masonry-Infilled  
574 RC Frames." *J. Struct. Eng.* 136(3): 285-296.

575 Vlassis, A.G., Izzuddin, B.A., Elghazouli, A. Y., Nethercot D.A. 2008. “Progressive collapse of  
576 multi-storey buildings due to sudden column loss. Part II: Application.” *Eng. Struct.* 30(5): 1424-  
577 1438

578 Weng, J., Lee, C. K., Tan K. H. & Lim N. S. 2017. “Damage as-sessment for reinforced concrete  
579 frames subject to progressive collapse.” *Eng. Struct.* 149: 147–160.

580 Xavier, F.B., Macorini, L. Izzuddin, M.B. 2015. “Robustness of Multistory Buildings with Masonry  
581 Infill.” *J. Perform. Constr. Facil.* 29(5): B4014004.

582 Xiao, Y., Kunnath, S., Li, F.W., Zhao, Y.B., Lew, H.S., Bao, Y. 2015. “Collapse test of three-story  
583 half-scale reinforced concrete frame building.” *ACI Struct. J.* 112(4): 429-438.

584 Yu, J., Tan, K.H. 2013. “Experimental and numerical investigation on progressive collapse resistance  
585 of reinforced concrete beam column subassemblages.” *Eng. Struct.* 55:90–106.

586

587

588

589

590

591

592

593

594

595

596

597

598

599

600

601

602

603

604

605

606

607

608

609

610

611

612

614 **Table 1.** Experimental and numerical specimens and test set-up details.

Author	Specimen code	Type	Sotrey no.	Bays no.	Scale	Masonry type	Lateral constraint	Seismic detailing	Aspect ratio ( $l_b/h_c$ )
Li et al. (2019)	(no code)		1	2	1/3	Brick	two-sides (partial)	Yes	1.58
Qian and Li (2017)	WSS	Experimental	2	1	1/4	Brick	one-side (full)	Yes	2.41
Qian and Li (2017)	WNL		2	1	1/4	Brick	one-side (full)	No	3.28
Di Trapani et al. (2020a)	FEM-S1F-B500						no	Yes	1.02
	FEM-S1R-B500						two-sides (full)	Yes	1.02
	FEM-nS1F-B500						no	No	1.02
	FEM-nS1R-B500						two-sides (full)	No	1.02
	FEM-S2R-B500	Numerical	1	1	1/1	Clay hollow	two-sides (full)	Yes	2.04
	FEM-nS2F-B500						no	No	2.04
	FEM-nS2F-B200						no	No	1.83
	FEM-nS2F-B300						no	No	1.90
	FEM-nS2R-						two-sides (full)	No	1.90

615

616 **Table 2.** Geometric and mechanical details of experimental and numerical specimens and parameters for the  
617 identification of the equivalent strut width of S1 struts

Specimen reference	$t$ (mm)	$h_c$ (mm)	$h_c'$ (mm)	$l_b$ (mm)	$l_b'$ (mm)	$d$ (mm)	$b_{wc}$ (mm)	$h_{wc}$ (mm)	$b_{wb}$ (mm)	$h_{wb}$ (mm)	$E_{m2}$ (MPa)	$E_{m1}$ (MPa)	$\tilde{E}_m$ (MPa)	$E_c$ (MPa)	$\lambda^*$ -	$w$ (mm)
Li et al. (2019)	63.5	950	1100	1500	1700	2025	200	200	100	150	5376	7680	6426	35725	3.170	274.5
Qian and Li (2017) - WSS	65	685	825	1650	1800	1980	150	150	90	140	4410	6300	5271	32837	7.191	156.1
Qian and Li (2017) - WNL	65	685	825	2250	2400	2538	150	150	90	140	4410	6300	5271	32837	16.915	129.4
FEM-S1F-B500	300	2670	3170	2720	3440	4678	720	300	300	500	6401	5032	5675	31476	1.659	1080.8
FEM-S1R-B500	300	2670	3170	2720	3440	4678	720	300	300	500	6401	5032	5675	31476	1.659	1080.8
FEM-nS1F-B500	300	2670	3170	2720	3440	4678	720	300	300	500	6401	5032	5675	31476	1.659	1080.8
FEM-nS1R-B500	300	2670	3170	2720	3440	4678	720	300	300	500	6401	5032	5675	31476	1.659	1080.8
FEM-S2R-B500	300	2670	3170	5440	6160	6928	720	300	300	500	6401	5032	5675	31476	8.587	629.0
FEM-nS2F-B500	300	2670	3170	5440	6160	6928	720	300	300	500	6401	5032	5675	31476	8.587	629.0
FEM-nS2F-B200	300	2970	3170	5440	6160	6928	720	300	1000	200	6401	5032	5675	31476	6.490	729.0
FEM-nS2F-B300	300	2870	3170	5440	6160	6928	720	300	700	300	6401	5032	5675	31476	6.190	709.4
FEM-nS2R-B300	300	2870	3170	5440	6160	6928	720	300	700	300	6401	5032	5675	31476	6.190	709.4

618

619 **Table 3.** Masonry infill material properties and parameters for the determination of the nominal stress-strain  
620 response of S1 struts

Specimen reference	$f_{vm}$ (MPa)	$f_{m2}$ (MPa)	$f_{m1}$ (MPa)	$\tilde{f}_m$ (MPa)	$\alpha$ -	$\beta$ -	$\gamma$ -	$\delta$ -	$f_{md0}$ (MPa)	$f_{mdu}$ (MPa)	$\varepsilon_{md0}$ -	$\varepsilon_{mdu}$ -
Li et al. (2019)	1.08	8.96	12.8	10.71	2.47E+06	4.08	0.00390	0.003823	4.22	0.49	0.000662	0.00803
Qian and Li (2017) - WSS	1.10	7.35	10.5	8.78	1.25E+06	2.52	0.00271	0.003237	4.21	0.42	0.000583	0.00859
Qian and Li (2017) - WNL	1.10	7.35	10.5	8.78	1.19E+06	1.65	0.00366	0.003594	4.27	0.43	0.000647	0.00844
FEM-S1F-B500	1.07	4.18	8.66	6.02	1.07E+07	16.77	0.05008	0.009042	1.56	1.03	0.001605	0.00713
FEM-S1R-B500	1.07	4.18	8.66	6.02	1.07E+07	16.77	0.05008	0.009042	1.56	1.03	0.001605	0.00713
FEM-nS1F-B500	1.07	4.18	8.66	6.02	1.07E+07	16.77	0.05008	0.009042	1.56	1.03	0.001605	0.00713
FEM-nS1R-B500	1.07	4.18	8.66	6.02	1.07E+07	16.77	0.05008	0.009042	1.56	1.03	0.001605	0.00713
FEM-S2R-B500	1.07	4.18	8.66	6.02	8.93E+06	6.83	0.00658	0.004471	1.64	0.38	0.000794	0.00802
FEM-nS2F-B500	1.07	4.18	8.66	6.02	8.93E+06	6.83	0.00658	0.004471	1.64	0.38	0.000794	0.00802
FEM-nS2F-B200	1.07	4.18	8.66	6.02	9.84E+06	7.76	0.00878	0.004942	1.59	0.44	0.000877	0.00789
FEM-nS2F-B300	1.07	4.18	8.66	6.02	1.00E+07	7.53	0.00811	0.004808	1.59	0.42	0.000853	0.00792
FEM-nS2R-B300	1.07	4.18	8.66	6.02	1.00E+07	7.53	0.00811	0.004808	1.59	0.42	0.000853	0.00792

621

622

623

624

625 **Table 4.** Parameters after the calibration  $\alpha_b$  and  $\xi$  and resulting dimensional properties.

Specimen reference	$\alpha_b$	$\xi$	$\alpha_b \cdot l_b$	$\tilde{f}_{md0} = \xi \cdot f_{md0}$	$\tilde{f}_{mdu} = \xi \cdot f_{mdu}$
	-	-	(mm)	(MPa)	(MPa)
Li et al. (2019)	0.500	1	750	4.22	0.49
Qian and Li (2017) - WSS	0.200	0.75	330	3.16	0.32
Qian and Li (2017) - WNL	0.500	0.85	1125	3.63	0.36
FEM-S1F-B500	0.250	0.90	680	1.40	0.93
FEM-S1R-B500	0.200	1.00	544	1.56	1.03
FEM-nS1F-B500	0.500	0.85	1360	1.32	0.87
FEM-nS1R-B500	0.300	1.00	816	1.56	1.03
FEM-S2R-B500	0.200	0.60	1088	0.98	0.23
FEM-nS2F-B500	0.200	0.50	1088	0.82	0.19
FEM-nS2F-B200	0.200	0.25	1088	0.40	0.11
FEM-nS2F-B300	0.150	0.25	816	0.40	0.10
FEM-nS2R-B300	0.150	0.40	816	0.63	0.17

626

627 **Table 5.** Parameters  $\kappa$  and  $\rho$  and associated data for their determination.

Specimen reference	$K_f$	$K_s$	$\kappa$	$N_{bmax}$	$R_f$	$R_s$	$\rho$	$\theta$
	(kN/m)	(kN/m)	-	(kN)	(kN)	(kN)	-	(°)
Li et al. (2019)	10717.5	45079.7	0.94	34.51	39.70	79.86	0.50	32.91
Qian and Li (2017) - WSS	8123.5	36781.2	0.97	17.31	67.03	58.13	1.15	27.00
Qian and Li (2017) - WNL	3203.7	22151.3	0.74	9.82	26.61	51.56	0.52	25.00
FEM-S1F-B500	117309.0	266586.3	1.05	80.53	478.24	615.59	0.78	42.66
FEM-S1R-B500	234618.0	533172.5	1.05	1084.00	977.65	683.99	1.43	42.66
FEM-nS1F-B500	117309.0	266586.3	1.05	35.00	214.12	581.39	0.37	42.66
FEM-nS1R-B500	234618.0	533172.5	1.05	943.00	697.06	683.99	1.02	42.66
FEM-S2R-B500	29327.3	141476.0	0.70	871.00	453.42	169.68	2.67	27.23
FEM-nS2F-B500	14663.6	70738.0	0.70	104.18	218.80	141.40	1.55	27.23
FEM-nS2F-B200	3128.2	81981.7	0.12	41.61	164.46	79.68	2.06	27.23
FEM-nS2F-B300	7390.5	79771.9	0.30	84.92	222.35	77.17	2.88	27.23
FEM-nS2R-B300	14780.9	159543.8	0.30	1040.00	375.07	123.48	3.04	27.23

628

629

630 **Table 6.** Experimental and numerical blind test specimens and test set-up details.

Author	Specimen code	Type	Storey no.	Bays no.	Scale	Masonry type	Lateral constraint	Seismic detailing	Aspect ratio ( $l_b/h_c$ )
Qian and Li (2017)	WNS	Experimental	2	1	1/4	Brick	one-side (full)	No	2.41
Di Trapani et al. (2020a)	FEM-S2F-B500	Numerical	1	1	1/1	Clay hollow	no	Yes	2.04
	two-sides (full)						No	2.04	
	two-sides (full)						No	1.83	

631 **Table 7** Geometric and mechanical details of experimental and numerical blind test specimens and parameters

632 for the identification of the equivalent strut width of S1 struts

Specimen reference	$t$	$h_c$	$h_c'$	$l_b$	$l_b'$	$d$	$b_{wc}$	$h_{wc}$	$b_{wb}$	$h_{wb}$	$E_{m2}$	$E_{m1}$	$\tilde{E}_m$	$E_c$	$\lambda^*$	$w$
	(mm)	(mm)	(mm)	(mm)	(mm)	(mm)	(mm)	(mm)	(mm)	(mm)	(MPa)	(MPa)	(MPa)	(MPa)	-	(mm)
Qian and Li (2017) - WNS	65	685	825	1650	1800	1980	150	150	90	140	4410	6300	5271	32837	7.191	156.1
FEM-S2F-B500	300	2670	3170	5440	6160	6928	720	300	300	500	6401	5032	5675	31476	8.587	629.0
FEM-nS2R-B500	300	2670	3170	5440	6160	6928	720	300	300	500	6401	5032	5675	31476	8.587	629.0
FEM-nS2R-B200	300	2970	3170	5440	6160	6928	720	300	1000	200	6401	5032	5675	31476	6.490	729.0

633

634

635  
636  
637

**Table 8.** Masonry infill material properties and parameters for the determination of the nominal stress-strain response of S1 struts for the blind test specimens.

Specimen reference	$f_{vm}$ (MPa)	$f_{m2}$ (MPa)	$f_{m1}$ (MPa)	$\tilde{f}_m$ (MPa)	$\alpha$ -	$\beta$ -	$\gamma$ -	$\delta$ -	$f_{md0}$ (MPa)	$f_{mdu}$ (MPa)	$\varepsilon_{md0}$ -	$\varepsilon_{mdu}$ -
Qian and Li (2017) - WNS	1.1	7.35	10.5	8.78	1.25E+06	2.52	0.00271	0.003237	4.21	0.42	0.000583	0.00859
FEM-S2F-B500	1.07	4.18	8.66	6.02	8.93E+06	6.83	0.00658	0.004471	1.64	0.38	0.000794	0.008018
FEM-nS2R-B500	1.07	4.18	8.66	6.02	8.93E+06	6.83	0.00658	0.004471	1.64	0.38	0.000794	0.008018
FEM-nS2R-B200	1.07	4.18	8.66	6.02	9.84E+06	7.76	0.00878	0.004942	1.59	0.44	0.000877	0.007885

638  
639

**Table 9.** Parameters  $\kappa$  and  $\rho$  and associated data for their determination.

Specimen reference	$K_f$ (kN/m)	$K_s$ (kN/m)	$\kappa$ -	$v_{b,max}$ -	$N_{b,max}$ (kN)	$R_f$ (kN)	$R_s$ (kN)	$\rho$ -	$\theta$ (°)
Qian and Li (2017) - WNS	8123	39377	0.90	0.034	14.36	38.40	66.38	0.58	29.08
FEM-S2F-B500	14663	70738	0.70	0.036	135.33	256.91	164.02	1.57	27.23
FEM-nS2R-B500	29327	141476	0.70	0.20	757.41	396.03	164.02	2.41	27.23
FEM-nS2R-B200	6256	163963	0.12	0.11	547.79	215.66	79.68	2.71	27.23

640  
641

**Table 10.** Parameters  $\alpha_b$  and  $\xi$  and resulting dimensional properties.

Specimen reference	$\alpha_b$ -	$\xi$ -	$\alpha_b \cdot l_b$ (mm)	$\tilde{f}_{md0} = \xi \cdot f_{md0}$ (MPa)	$\tilde{f}_{mdu} = \xi \cdot f_{mdu}$ (MPa)
Qian et al. (2017) - WNS	0.42	0.800	693	3.37	0.34
FEM-S2F-B500	0.19	0.580	1033.6	0.95	0.22
FEM-nS2R-B500	0.20	0.580	1088	0.95	0.22
FEM-nS2R-B200	0.18	0.250	979.2	0.40	0.11

642

**Table 11.** Geometric and mechanical properties of the infilled frames of the sample strut.

$t$ (mm)	$h_c$ (mm)	$h_c'$ (mm)	$l_b$ (mm)	$l_b'$ (mm)	$d$ (mm)	$b_{wc}$ (mm)	$h_{wc}$ (mm)	$b_{wb}$ (mm)	$h_{wb}$ (mm)	$E_{m2}$ (MPa)	$E_{m1}$ (MPa)	$\tilde{E}_m$ (MPa)	$f_{vm}$ (MPa)	$f_{m2}$ (MPa)	$f_{m1}$ (MPa)	$\tilde{f}_m$ (MPa)
300	2900	3400	5900	6300	7159	400	800	300	500	6401	5032	5675	1.07	8.66	4.18	6.02

644

**Table 12.** Reinforcement details for the central span beams.

Section	Stories 1-2-3		Stories 4-5-6	
	Top reinforcement	Bottom reinforcement	Top reinforcement	Bottom reinforcement
1-1	7 $\phi$ 16	4 $\phi$ 16	6 $\phi$ 16	3 $\phi$ 16
2-2	7 $\phi$ 16	4 $\phi$ 16	6 $\phi$ 16	3 $\phi$ 16

646  
647  
648

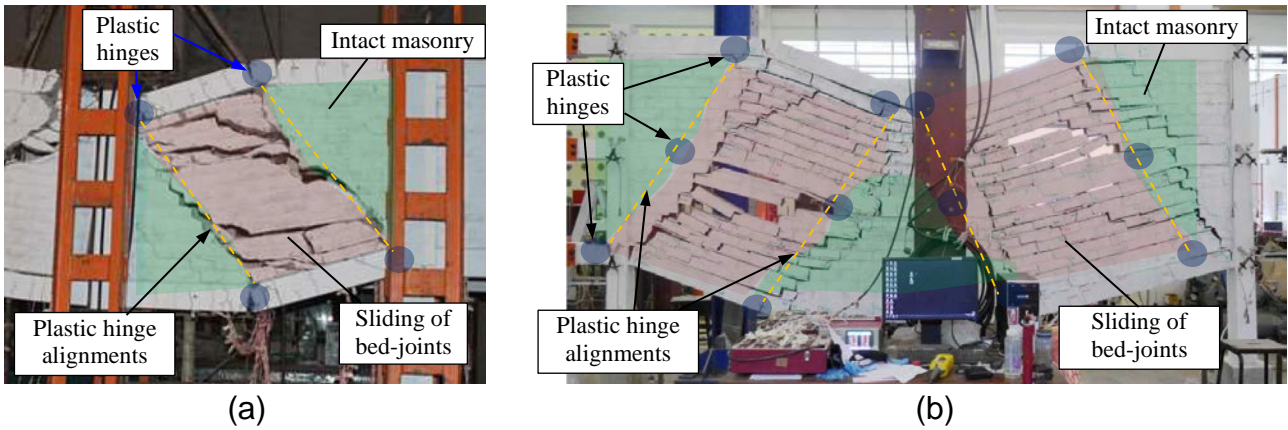


**Fig. 1.** Interpretation of the damage mechanism in pushdown tests of infilled frames: a) One-story infilled frame (Li et al. 2019); b) Two-story infilled frame (Qian and Li 2017).

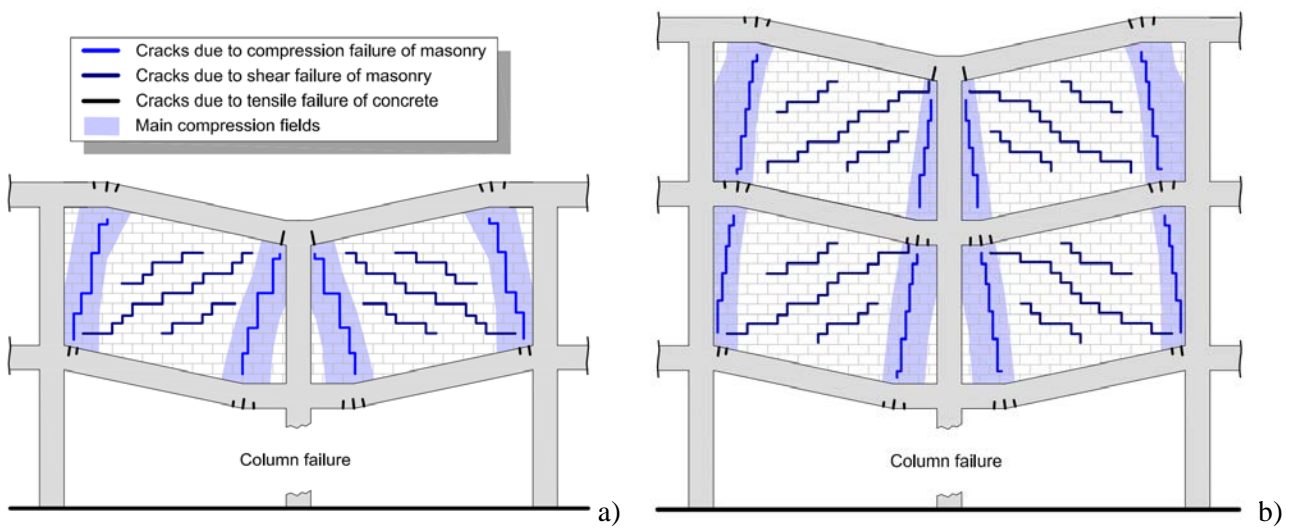


**Fig. 2.** Typical damage mechanisms associated with progressive collapse of infilled frames: a) One-story infilled frames; b) Multi-story infilled frames.

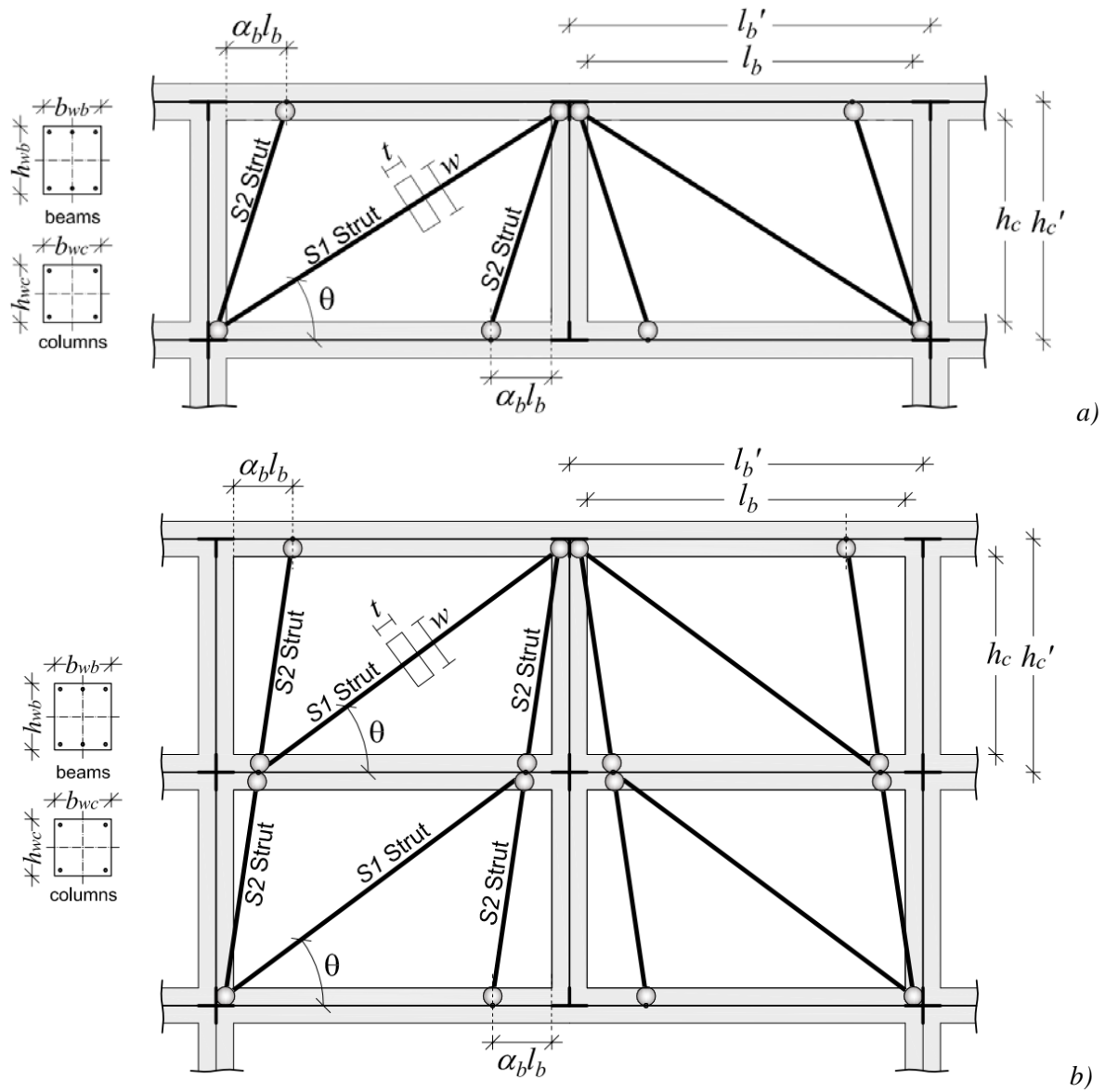


**Fig. 3.** Proposed equivalent strut model for: a) One-storey infilled frames; b) Multi-storey infilled frames.

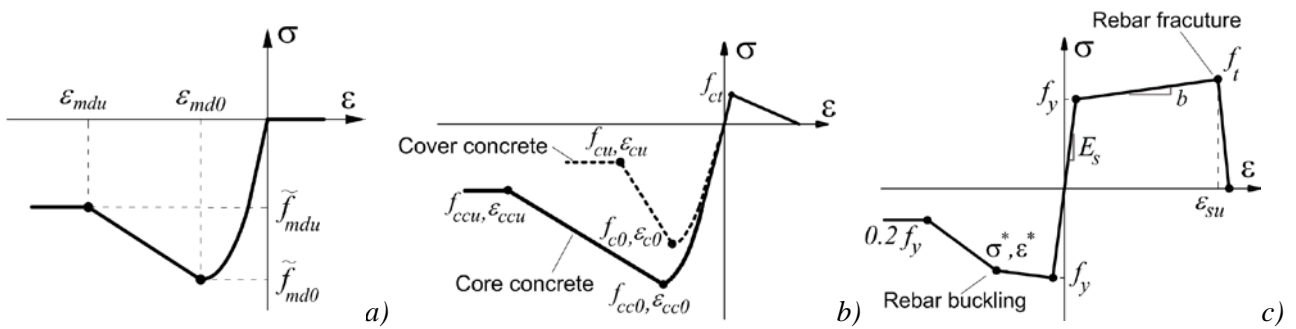


**Fig. 4.** Adopted stress-strain model for: a) S1 struts; b) Confined and unconfined concrete; c) Rebars.

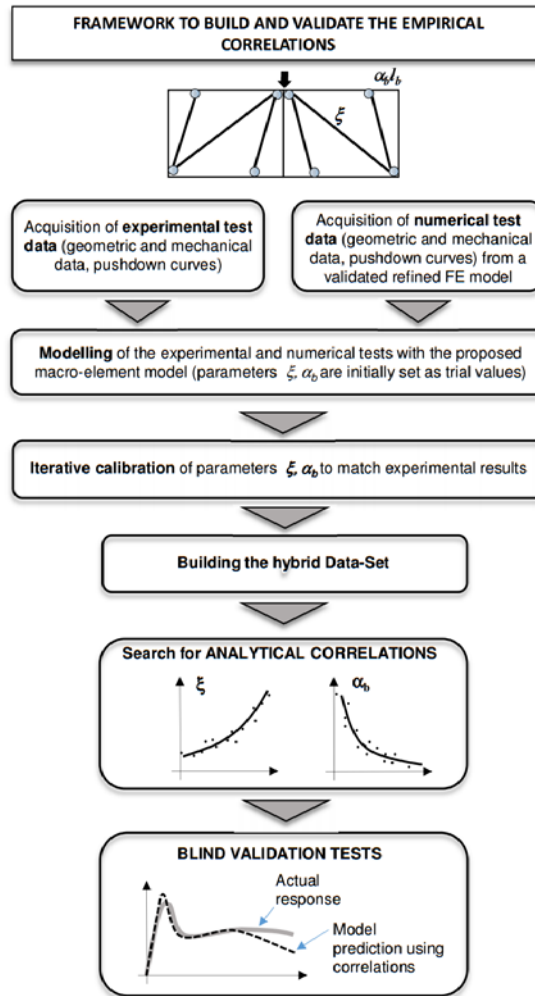


**Figure 5:** Framework to build and validate the empirical correlations.



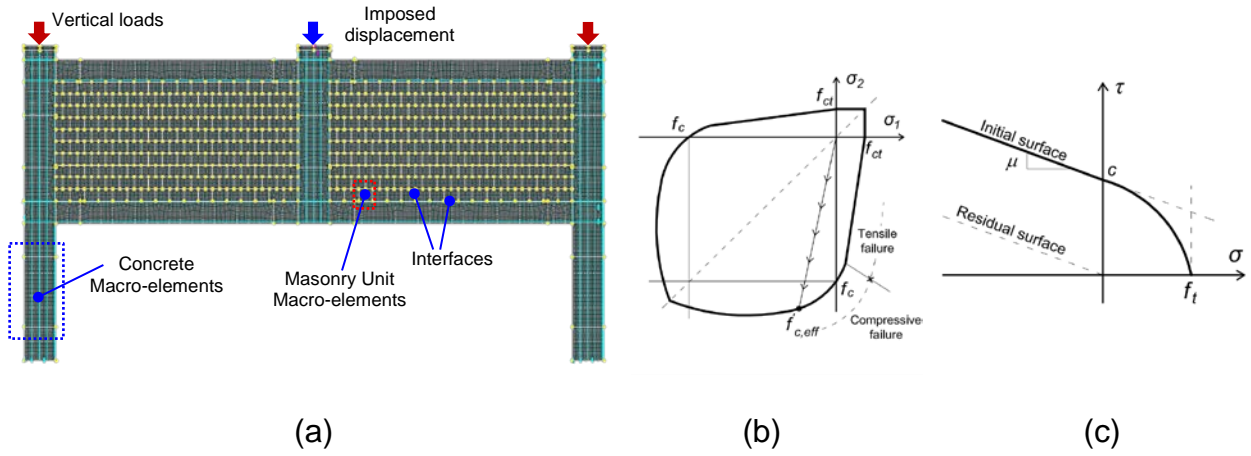


**Figure 6:** Refined FE model (Di Trapani et al. 2020): a) Overall assembly of the model; b) Concrete and masonry macro-elements failure surface; c) interfaces failure surface.

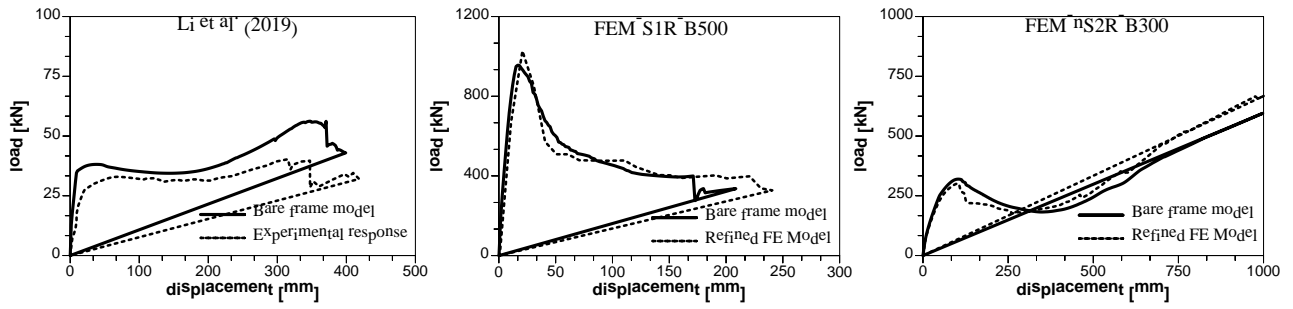


Fig. 7. Bare frame experimental and numerical pushdown curves and model predictions.

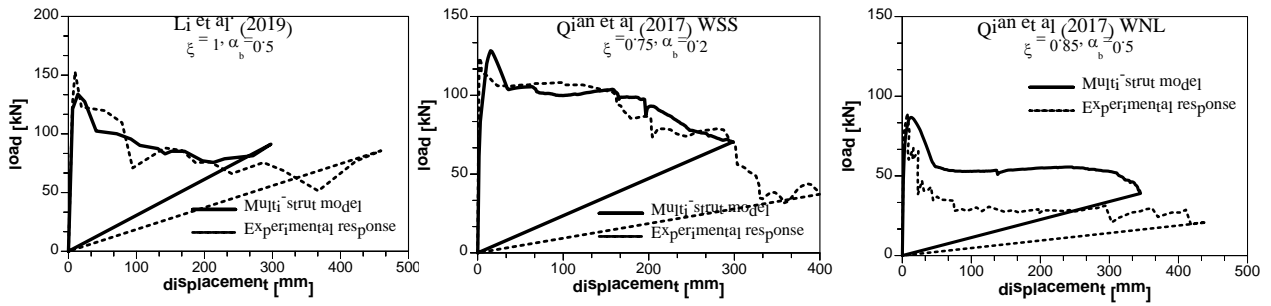
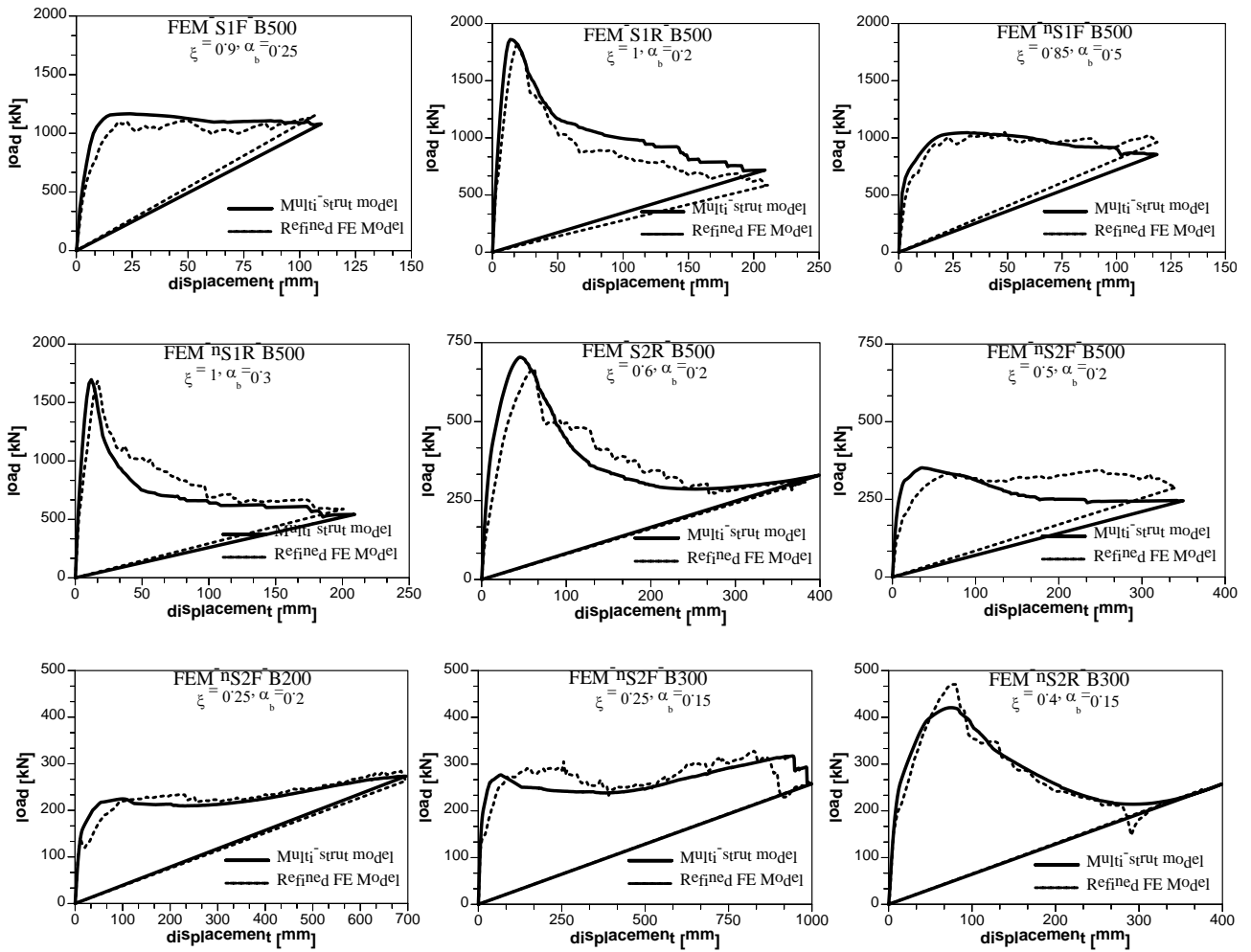
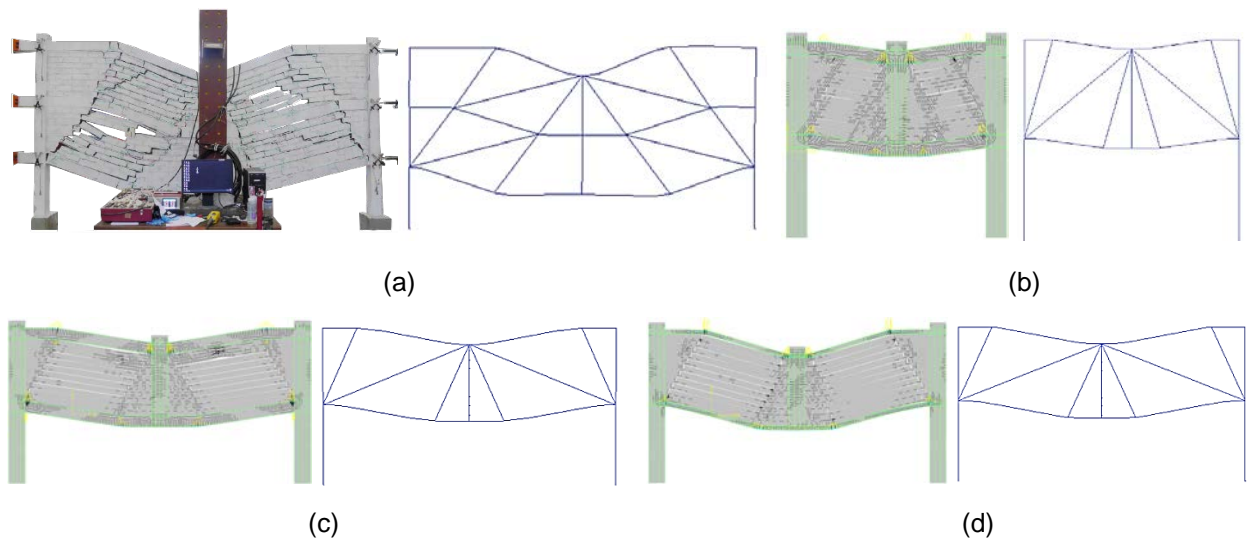


Fig. 8. Experimental pushdown curves and proposed model pushdown curves at the end of the calibration.



**Fig. 9.** Numerical pushdown curves from the refined FE model and proposed model pushdown curves at the end of the calibration.



**Fig. 10.** Comparison between the deformed shapes of experimental and numerical specimens and those obtained after the equivalent strut models calibration: a) Qian and Li (2017) – WNL; b) FEM-S1R-B500; c) FEM-S2R-B500; d) FEM-nS2F-B200

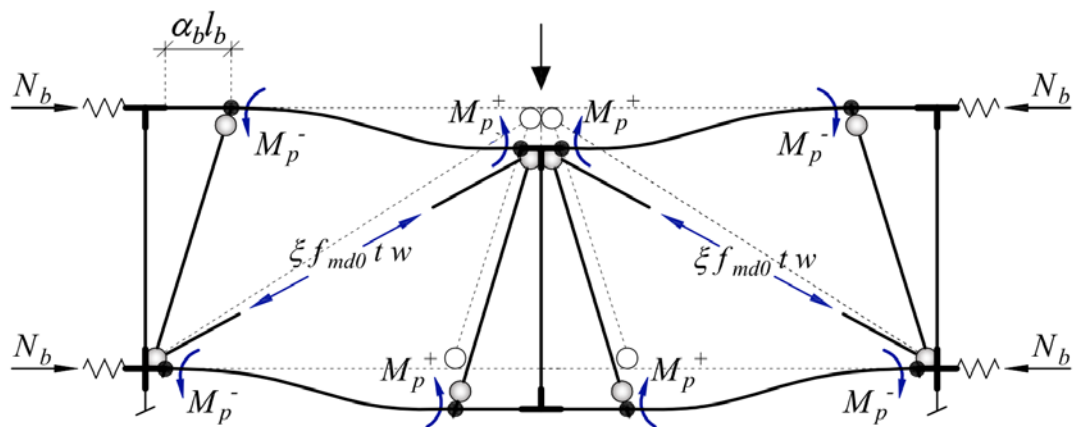


**Fig. 11.** Typical collapse mechanism of the proposed equivalent strut model (sample for a one-storey infilled frame).

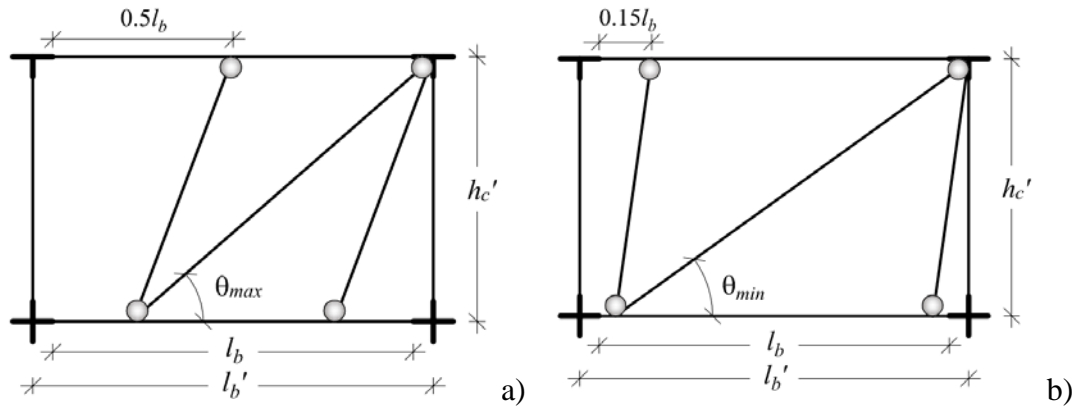


**Fig. 12.** Limit configurations of the equivalent strut model for the estimation of the average angle of inclination of S1 strut in multi-storey infilled frames: a)  $\theta_{max}$  configuration; b)  $\theta_{min}$  configuration.

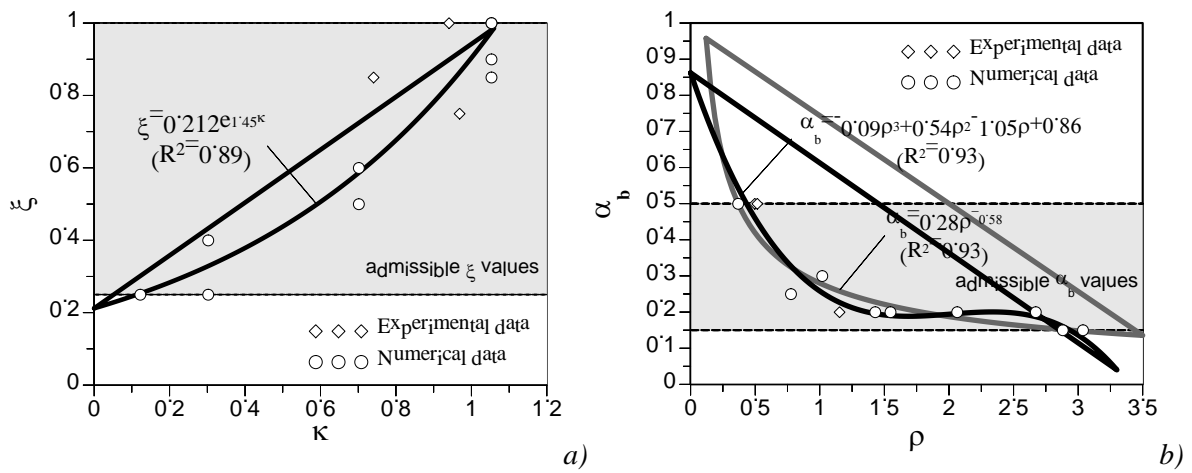


**Fig. 13.** Experimental and numerical data and analytical correlations: a)  $\xi-\kappa$ ; b)  $\alpha_b-\rho$ .

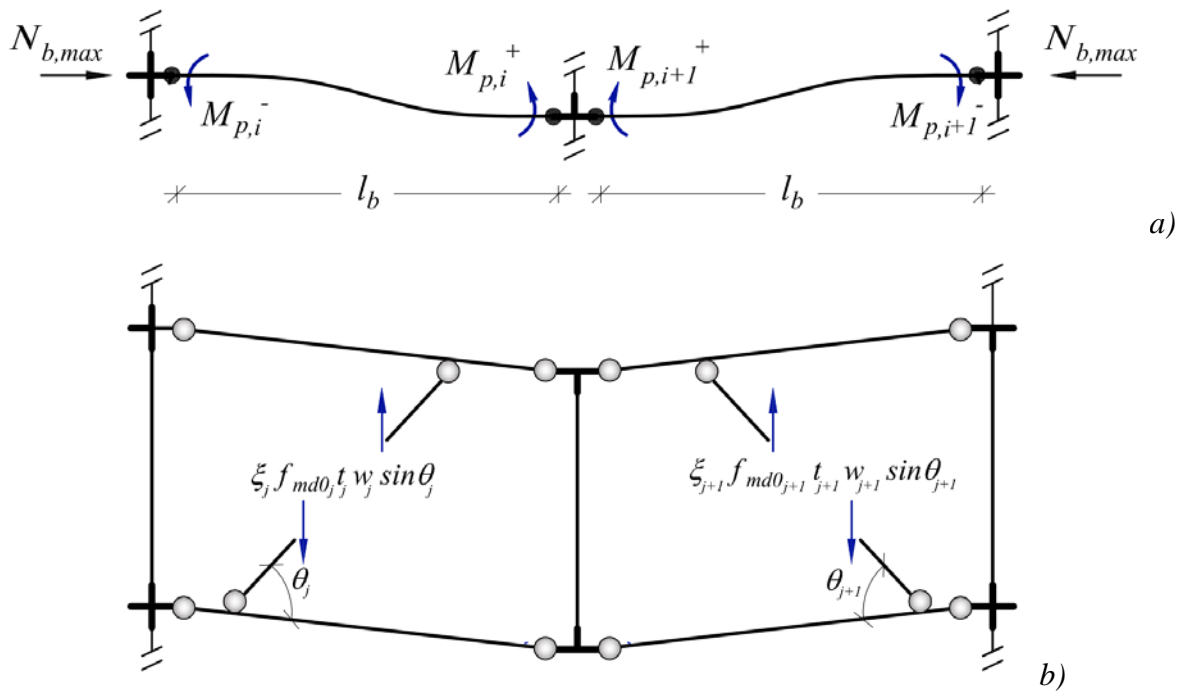


**Fig. 14.** Simplified limit equilibrium schemes for the evaluation of: a)  $R_f$ ; b)  $R_s$ .

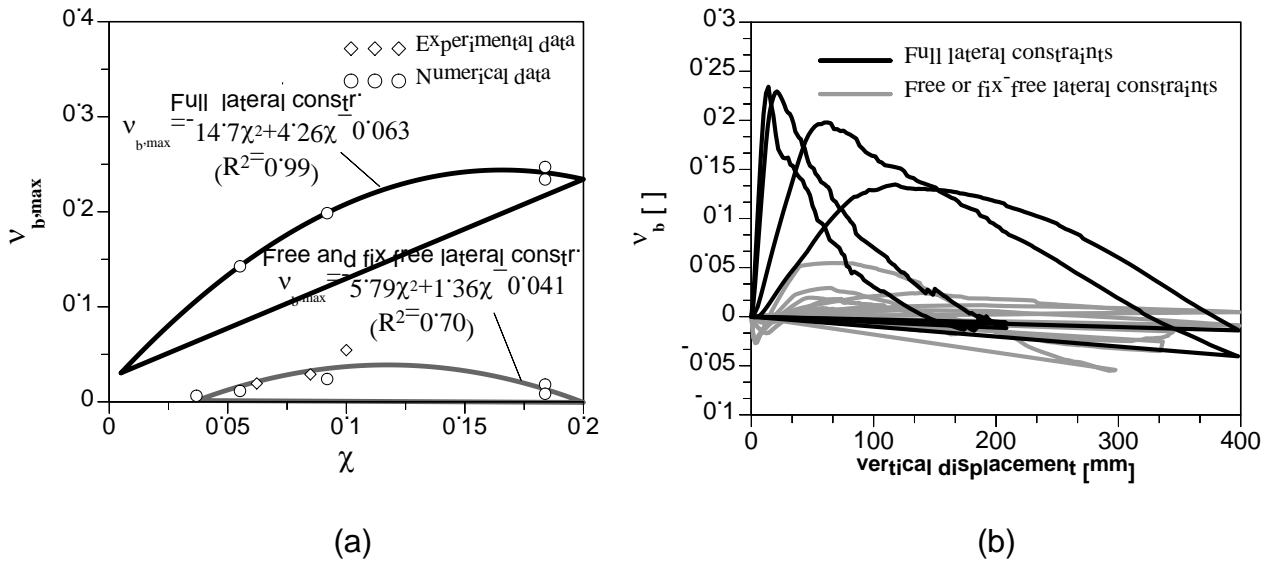


**Fig. 15.** Average dimensionless axial forces in beams: a) experimental and numerical data and analytical correlations with the and the height-to-length ratio ( $\chi$ ) for different lateral restraint conditions; b) variation with the vertical displacement.

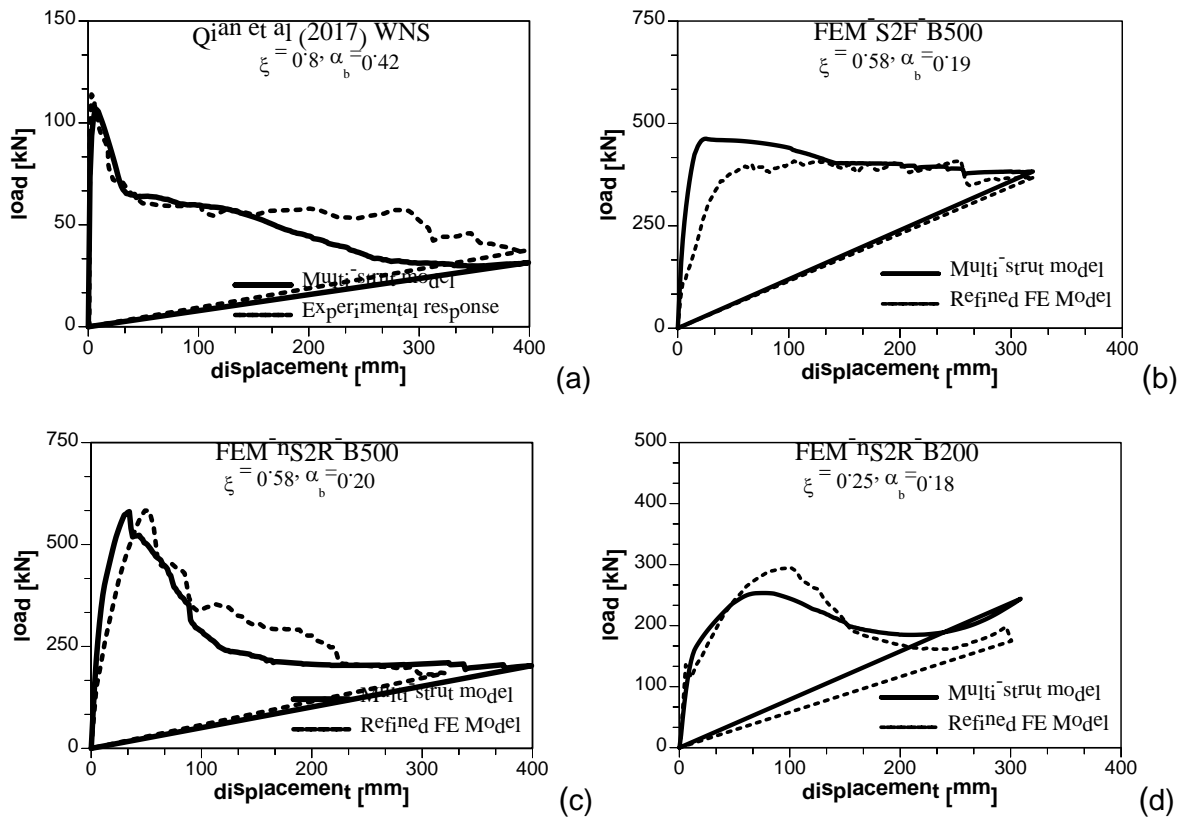


**Figure 16.** Blind validation tests of the proposed model with experimental and numerical test results.

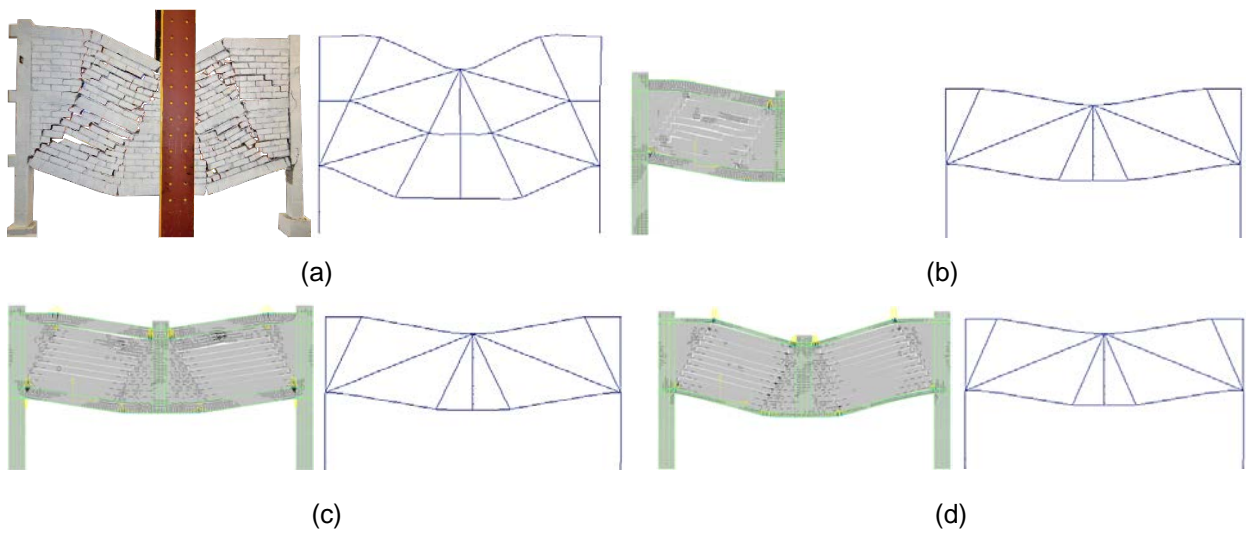


**Fig. 17.** Comparison between the deformed shapes of experimental and numerical blind test specimens and those predicted by the model: a) Qian and Li (2017) – WNS; b) FEM-S2F-B500; c) FEM-nS2R-B500; d) FEM-nS2R-B200

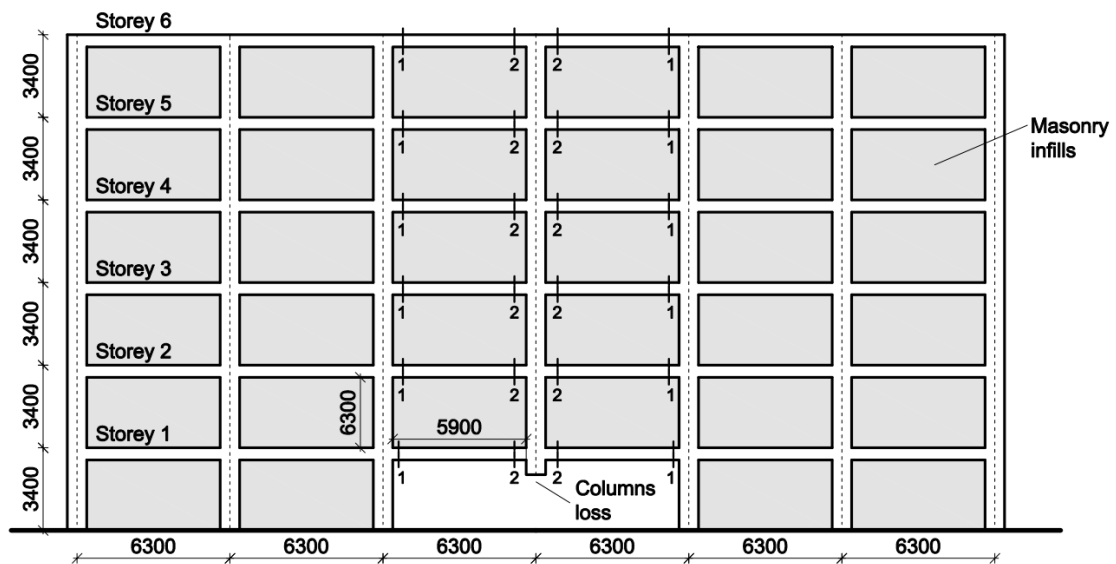


**Fig. 18.** Sample structure geometry (dimensions in mm).

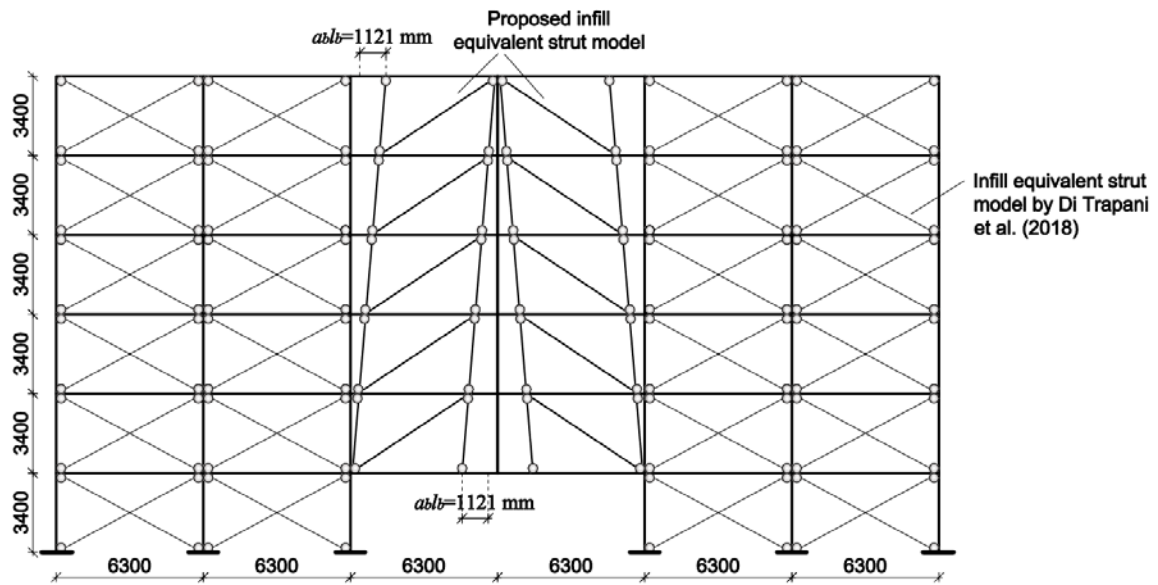


**Fig. 19.** Sample structure multi-strut progressive collapse model (dimensions in mm).

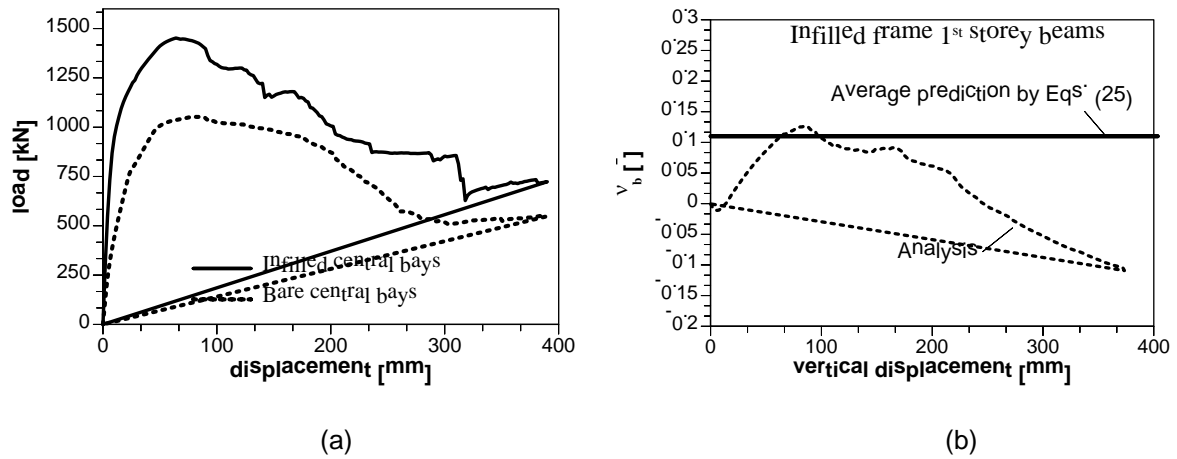


**Fig. 20.** Results of the pushdown tests: a) comparison between pushdown responses of the model with and without infills in the central bays; b) Dimensionless axial force in first storey beams for the model with the infills in the central bays.

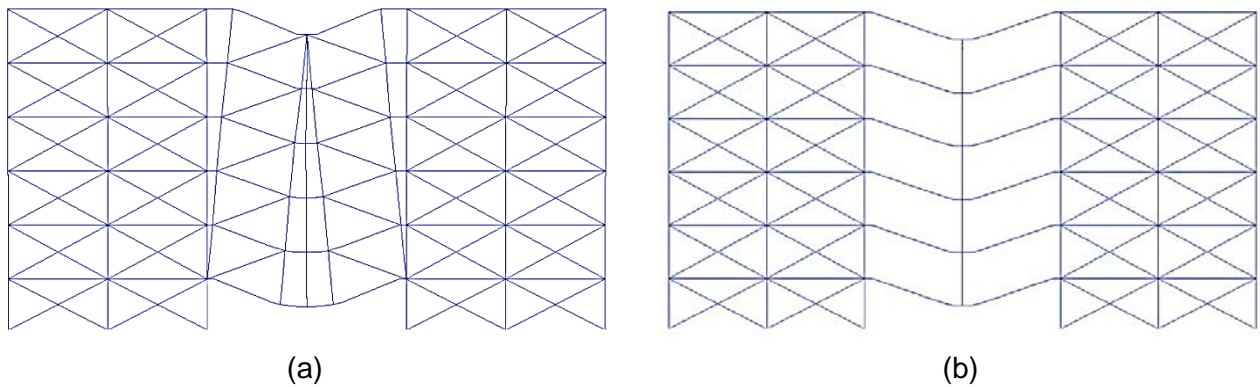


**Fig. 21.** Deformed shapes of the models during the pushdown tests: a) Infilled central bays; b) Bare central bays.



